

Robust Simulation of Sharp-Interface Models for Fast Estimation of CO₂ Trapping Capacity in Large-Scale Aquifer Systems

Halvor Møll Nilsen^a, Knut-Andreas Lie^a, Odd Andersen^{a,b,*}

^a*SINTEF ICT, Applied Mathematics, P.O. Box 124 Blindern, N-0314 Oslo, Norway*

^b*University of Bergen, Dept. Math., P.O. Box 7803, N-5020 Bergen, Norway*

Abstract

Modeling geological carbon storage represents a new and substantial challenge for the subsurface geosciences. To increase understanding and make good engineering decisions, containment processes and large-scale storage operations must be simulated in a thousand-year perspective. Large differences in spatial and temporal scales makes it prohibitively expensive to compute the fate of injected CO₂ using traditional 3D simulators. Instead, accurate forecast can be computed using simplified models that are adapted to the specific setting of the buoyancy-driven migration of the light fluid phase.

This paper presents a family of vertically integrated models for studying the combined large-scale and long-term effects of structural, residual, and solubility trapping of CO₂. The models are based on an assumption of a sharp interface separating CO₂ and brine and can provide a detailed inventory of the injected CO₂ volumes over periods of thousands of years within reasonable computational time. To be compatible with simulation tools used in industry, the models are formulated in a black-oil framework. The models are implemented in MRST-co2lab, which is an open community software developed especially to study and optimize large-scale, long-term geological storage of CO₂. The resulting simulators are fully implicit and handle input from standard geomodeling tools.

Keywords: CO₂ storage, vertical equilibrium, compressibility, dissolution

*Please address correspondence to O. Andersen

Email addresses: Halvor.M.Nilsen@sintef.no (Halvor Møll Nilsen), Knut-Andreas.Lie@sintef.no (Knut-Andreas Lie), Odd.Andersen@sintef.no (Odd Andersen)

1. Introduction

Dipping saline aquifers comprise the largest volumes available for large-scale storage of CO_2 . To accurately estimate the storage capacity of an open aquifer, one must determine the maximum amount of CO_2 that can be injected and how far and how fast the injected plume will migrate throughout the aquifer. The injection and migration processes are governed by delicate balances of various physical mechanisms (see Figure 1) which may change with time and spatial location. Resolving these processes is a challenging multiscale problem that involves a large disparity in spatial and temporal scales. CO_2 is very mobile and can travel large distances, but the flow is usually confined to thin layers underneath a sealing caprock or other low-permeable vertical barriers. A typical saline aquifer considered for CO_2 storage can be viewed as a thin, slightly inclined sheet that spans thousands of square kilometers. This, in combination with differences in density between the supercritical CO_2 plume and the resident brine, means that the vertical fluid segregation will be almost instantaneous compared with the up-dip migration. The tendency of forming a relative flat fluid interface is an effect of the pressure distribution, which in turn depends strongly on the flow in the vertical direction, particularly near the interface. The vertical fluid distribution must also be accurately represented to avoid introducing large errors in the forecast of the updip migration. (For nonlinear relative permeabilities, a large error will result from replacing the average of the mobility by the mobility of the average phase distribution). The thin plume and sharp transition between CO_2 and brine means that high vertical resolution is required to compute the vertical phase distribution. High grid resolution is also needed in the lateral direction to resolve the unstable dynamics of convective dissolution, which retards and limits the plume migration, and to account for small undulations in the caprock topography, that may both retard the migration of the plume and divert its path. In other words, simulating likely outcomes over a period of thousands of years is in most cases computationally intractable with conventional 3D reservoir simulators.

This is clearly demonstrated in the recent Stuttgart benchmark [1], in which a variety of commercial simulators and research codes were used by leading academic and industry experts to solve three model problems. Despite a large computational effort and significant work spent in eliminating differences in input data, the reported results are striking in their disparity, particularly for the study of how a supercritical CO_2 plume forms and mi-

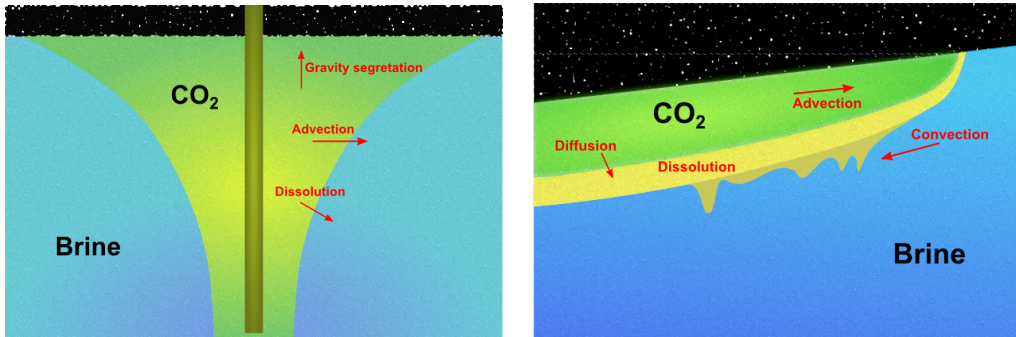


Figure 1: Illustration of injection and trapping of CO_2 under a sealing caprock. The plots show forces active during the injection (left) and migration phase (right).

grates upward in a small region of the Johansen formation [2, 3] from the Norwegian North Sea. At the end of simulation, the reported results show almost no consensus in the simulated shapes of the CO_2 plume.

In our opinion, there is an urgent need to advance state-of-the-art in numerical simulation to improve the assessment of storage capacity, facilitate approval of specific storage projects, and help realize the storage potential both globally and locally on the Norwegian Continental Shelf. In terms of modeling, efforts are needed along several parallel paths. First, one must continue to develop reliable numerical methods that model fundamental flow physics accurately and correctly. Second, these methods must be combined in robust numerical formulations that account for varying degrees of coupling between the different physical effects that drive or influence CO_2 migration. These numerical formulations need to be sufficiently flexible so that one in a simple and case-dependent manner can combine the flow equations with thermal, geomechanical, and geochemical effects. Finally, the formulations must be implemented as trustworthy software that enables transparent comparisons of models, methods, and simulated outcomes.

We believe that the only way these challenges can be tackled is through collaboration, development and extensive use of community software. To contribute to this, and to accelerate transfer of knowledge developed in academic research projects to end-users in industry and the public sector, we have started developing a community software called `MRST-co2lab` [4, 5, 6, 7, 8] implemented on top of the open-source Matlab Reservoir Simulation Toolbox (MRST) [9, 10, 11, 12]. Both MRST and its CO_2 module can be freely downloaded and used under the GNU General Public License v3.0. The soft-

ware offers reliable modeling of realistic storage scenarios, enables interactive experimentation with various model assumptions like boundary conditions, fluid models and parameters, injection points and rates, amount of subscale trapping, and so on, and simplifies the development, implementation, and comparison of new models and computational methods. The software offers a hierarchy of models and tools of increasing computational complexity [7, 8], as well as a set of tutorials and examples that demonstrate and highlight how these tools can be applied to study fundamental flow physics as well as descriptions of realistic storage scenarios based on public data sets of the Johansen formation [3, 2], the Sleipner injection [13], and saline aquifers from the Norwegian Continental Shelf [14].

Herein, we present a family of vertically-integrated models for studying the combined large-scale and long-term effects of structural, residual, and solubility trapping to provide detailed inventories of injected CO₂ volumes over periods of thousands of years. All models are based on the assumption of vertical equilibrium (VE) with a sharp interface that separates the injected CO₂ from the resident brine. Apart from the open-source implementation, the novelty of our work lies in a flexible and robust formulation that unifies work from the early period of reservoir simulation [15, 16, 17, 18], when practical numerical aspects were primarily in focus, with recent extensions of the VE framework [19] that focus more on physical effects related to large-scale CO₂ injection. The validity of the simplifying assumptions underlying VE models has been studied both with respect to spatial [20] and temporal [21] scales, and the utility of VE models is thoroughly discussed in, e.g., [22, 23]. Early studies focused on VE models with a sharp-interface assumption [24, 25, 26], and models that only account for the basic effects of buoyant migration were successfully used to simulate long-term migration in the Utsira [27] and Johansen [28] aquifers. Later, the class of VE models has been extended to incorporate most of the flow effects that are pertinent to large-scale migration, including compressibility [29], convective dissolution [30, 31], capillary fringe [32], small-scale caprock topography variations [33, 34, 35], various hysteretic effects [36, 37, 38], multiple geological layers [39, 40], and heat transfer [41]. In particular, several studies show that vertical equilibrium simulations compare well with 3D simulators on case studies of the Johansen aquifer [42] and the 9th layer of the Sleipner injection [27, 43]. The assumption of vertical equilibrium not only reduces the number of spatial dimensions, and hence the number of grid cells, but will also reduce the coupling between pressure and fluid transport and improves the character-

istic time constants of the problem [42]. As a results, VE simulations will typically be orders of magnitude faster and consume significantly less memory than conventional 3D simulators. In [43, 23], the authors report a simulation of CO₂ migration under the caprock at Sleipner, for which a VE simulator running for a few minutes on a single core produced forecasts with similar accuracy as a 3D simulation with TOUGH2 running for several hours on one hundred cores.

To develop our numerical framework, we first discuss modeling of various physical mechanisms including compressibility and retardation effects from subscale trapping. We then show how a general class of VE models can be recast as standard black-oil models using the traditional concept of pseudo-functions [44, 45, 46, 47], and discuss the inclusion of dynamic dissolution effects. In particular, we point out in detail the approximations and numerical considerations needed to obtain flexible and efficient numerical formulations that resolve the main physical effect well within the accuracy normally available from input data. The overall formulation is implemented as an extension of existing black-oil solvers in MRST [12], which in turn have been implemented using automatic differentiation and hence enable simple computation of gradients and parameter sensitivities, e.g., through an adjoint formulation. This enables users to easily perform sensitivity studies or formulate efficient strategies for rigorous mathematical optimization of large-scale injection strategies [48, 49, 7, 6]. In [50], we discuss how the framework can be extended to account for smooth transitions (capillary fringe) between pure CO₂ and brine. We also show how inclusion of more advanced flow physics naturally leads to pressure-dependence and hysteretic effects in the vertically-integrated relative permeabilities and capillary pressure, and suggest implementation choices we think are important to make flexible and efficient VE simulators.

Whereas the focus of the present paper is on reduced models, the functionality provided by MRST-co2lab also includes other computational tools for analysis of CO₂ storage. In [5], we discuss tools for fast and interactive estimation of structural trapping and potential migration paths under the assumption that CO₂ is injected at an infinitesimal rate. These tools do not account for temporal aspects, but will nevertheless reveal important information such as accessible structural traps, spill points and migration paths, good injection locations, points where the CO₂ may leak out through open boundaries, etc. In [6, 7, 8] we outline how the various tools can be combined to create a flexible tool chain for estimating storage capacities and

studying injection scenarios. In particular, we study and optimize strategies for injecting hundreds of megatonnes of CO₂ into various saline aquifers in the Norwegian North Sea using data sets from the recent CO₂ Storage Atlas [14]. Finally, we mention that MRST-co2lab also contains conventional 3D simulation capabilities and that work is in progress to include additional physics such as thermal, geochemical, and geomechanical effects.

Complete MATLAB scripts containing all the statements necessary to reproduce the figures presented in this paper can be downloaded as part of the 2015b release of MRST-co2lab.

2. Trapping mechanisms

With a sharp-interface VE model, it is simple to make accurate inventories of carbon trapping for specific scenarios, detailing how injected CO₂ volumes are separated into parts that can be considered safely contained and parts that may potentially leak back to the surface. The general trend is that CO₂ becomes more securely trapped with time as a result of trapping processes taking place at different rates that vary from days to years to thousands of years.

When CO₂ is injected into a deep subsurface rock formation, it forms a separate mobile, typically dense phase (the CO₂ plume) that invades the medium and displaces other liquids present in the pore space (typically: brine). The CO₂ phase is almost always less dense than the resident fluids and will therefore rise upwards and hence be replaced by other fluids. However, as the volume fraction of the CO₂ phase falls below a certain level, CO₂ becomes trapped in the pore space between rock grains by capillary pressure from the other fluids and stops flowing. This is referred to as *residual trapping* and the corresponding volumes of CO₂ are denoted '**residual**' in the inventory. At any point, the inventory of the plume is therefore subdivided into two categories: '**residual (plume)**' refers to the fraction of the CO₂ column that will eventually stay behind in a residually trapped state when the plume leaves its current position, whereas '**movable (plume)**' is the remaining part that is free to migrate away from the current position.

In most relevant scenarios, CO₂ is injected under a sealing rock in which the capillary pressure inside pore throats is greater than the buoyancy pressure of the CO₂. The top seal will prevent the direct upward movement of the plume and if the seal is sloping, the CO₂ will form a thin layer underneath that slowly migrates in the upslope direction until it encounters a

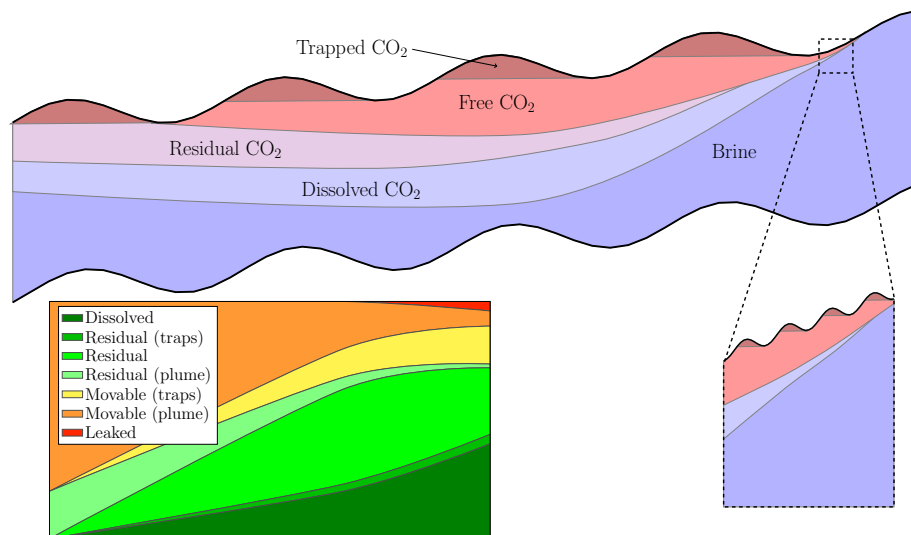


Figure 2: Schematic of a vertical section of an aquifer showing the different forms in which the injected CO_2 can be present during migration. The right inset shows small-scale undulations in the top surface which typically will not be resolved in a large-scale model. The left inset shows a detailed inventory of various categories of trapped CO_2 , stacked in terms of increasing leakage risk, as function of time from the end of injection.

structural trap, i.e., a fold in the top surface inside which the CO_2 will accumulate. Once inside a trap, the CO_2 will remain *structurally trapped* unless the height of the plume creates a capillary pressure that enables the CO_2 to enter the seal. The structurally trapped volumes are therefore divided into two similar categories: '**residual (traps)**' will remain immobile and never leak, while '**movable (traps)**' could in principle escape through a crack in the top seal. Once a trap is filled, the CO_2 will spill over and continue migrating upward. CO_2 can also be trapped in *stratigraphic traps* because of changes in rock type within the storage layer, but this mechanism is not represented in VE models.

The remaining trapping mechanisms are *solubility and mineral trapping*. Over time, CO_2 will dissolve in the resident fluids. Brine containing dissolved CO_2 is slightly denser than the surrounding fluids and will sink to the bottom of the rock formation, thereby trapping CO_2 more securely. This enables a mixing process that increasingly disperses CO_2 into brine over time. The dissolved CO_2 forms a weak carbonic acid that may react with the reservoir rock to form and precipitate carbonate minerals that bind CO_2 permanently

to the rock. This process may be rapid or very slow and is not accounted for herein.

To summarize, the 'dissolved', 'residual (traps)', and 'residual' volumes are safely stored unless changes occur in the aquifer that alter the residual saturation of CO₂ or cause the CO₂ to effervesce from the formation water (think of the fizz when you open a bottle of carbonated water). The 'movable (traps)' volumes are immobilized and will be safely stored unless the structural traps contain leakage points. The remaining volumes will continue to migrate in the upslope direction, the 'residual (plume)' volumes will eventually remain as residually trapped and only the 'movable (plume)' volumes may leak if not trapped by another trapping mechanism at a later time. If the aquifer model has open boundaries, some of the injected CO₂ may also leave the computational domain during the simulation and these volumes will, in lack of a better word, be referred to as '**leaked**'. We emphasize that this does not mean that the corresponding CO₂ has leaked back to the atmosphere; in most cases it will continue to migrate inside another rock volume that is outside the simulation model. In the inventory in Figure 2 the various categories of CO₂ volumes have been stacked according to increasing risk of leakage, from dissolved CO₂ (dark green color) to volumes that are still movable (yellow/orange) or have already left the simulated domain (red).

3. Derivation of the basic VE model

Let brine and CO₂ be wetting and non-wetting fluids, respectively, and assume incompressible rock and fluids, no capillary forces, and impermeable top and bottom of the aquifer. Then, mass conservation and Darcy's law read:

$$\frac{\partial}{\partial t}(\phi s_\alpha) + \nabla \cdot \vec{v}_\alpha = q_\alpha, \quad (1)$$

$$\vec{v}_\alpha = -\mathbf{k}\lambda_\alpha(\nabla p - \rho_\alpha \vec{g}). \quad (2)$$

Here, ϕ denotes porosity, \mathbf{k} permeability, p pressure, and \vec{g} the gravity vector, whereas s_α , λ_α , and q_α denote saturation, mobility, and volumetric source for phase $\alpha = \{w, n\}$.

We introduce a curvilinear coordinate system $(\vec{e}_\xi, \vec{e}_\eta, \vec{e}_\zeta)$ whose orientation is defined to align closely with the global system $(\vec{e}_x, \vec{e}_y, \vec{e}_z)$, but be slightly tilted so that \vec{e}_ζ locally is perpendicular to the main flow direction (disregarding small and medium-scale oscillations). The tilt only depends on

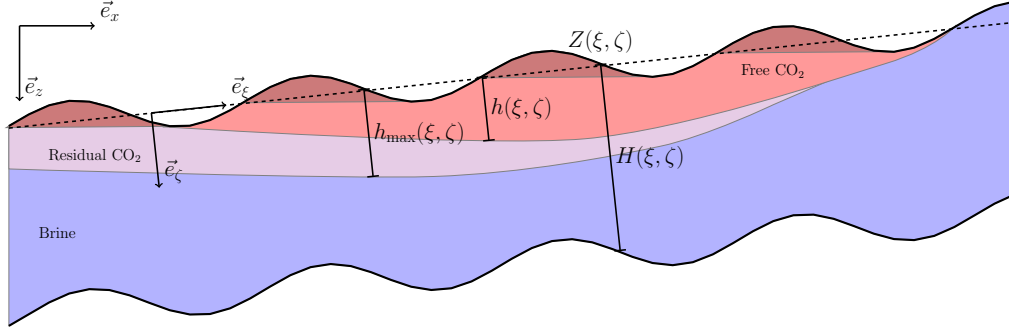


Figure 3: Schematic of the fluid distribution and the coordinate systems used to derive the basic vertical-equilibrium model. Here, $h(\xi, \eta)$ is the interface between CO_2 and brine, and h_{\max} represents the historical maximum value of h for a given location. The dashed line indicates assumed mean direction of flow within the aquifer (which is here illustrated as straight, but is allowed to be slightly curved in the general case).

ξ and η , is assumed to vary smoothly and at all points remain modest (a few degrees). We further write $\vec{g} = \vec{g}_{\parallel} + g_{\zeta} \vec{e}_{\zeta}$ and $\nabla = \nabla_{\parallel} + \vec{e}_{\zeta} \partial_{\zeta}$, where \parallel refers to the $(\vec{e}_{\xi}, \vec{e}_{\eta})$ components of a vector/operator. In the new coordinate system, the aquifer is described by the top surface $Z(\xi, \eta)$ and its thickness $H(\xi, \eta)$ in the ζ -direction, see Figure 3. Capital letters are used for quantities in the upscaled model.

Integrating (1) from top to bottom of the aquifer, neglecting distortions from the curvilinear nature of the coordinate system¹, we obtain:

$$\frac{\partial}{\partial t} \left[\int_Z^{Z+H} S_{\alpha} \phi d\zeta \right] + \nabla_{\parallel} \cdot \left[\int_Z^{Z+H} \vec{v}_{\alpha} d\zeta \right] = \int_Z^{Z+H} q_{\alpha} d\zeta. \quad (3)$$

By design of the coordinate system, the flow along \vec{e}_{ζ} will take place very rapidly compared with the migration in the $(\vec{e}_{\xi}, \vec{e}_{\eta})$ direction. Hence, we assume hydrostatic equilibrium in the \vec{e}_{ζ} direction. Since capillary pressure is neglected, CO_2 and brine will at equilibrium be separated by a sharp interface located a distance $h(\xi, \eta)$ from the caprock along \vec{e}_{ζ} . Setting the pressure datum P_Z at the top surface, the pressure at a given depth ζ is

¹A detailed explanation of the approximations related to the curvilinear system is provided in Appendix A.

determined by

$$p(\zeta) = \begin{cases} P_Z + \rho_n g_\zeta (\zeta - Z), & Z \leq \zeta \leq Z + h, \\ P_Z + \rho_n g_\zeta h + \rho_w g_\zeta (\zeta - Z - h), & Z + h \leq \zeta \leq Z + H. \end{cases} \quad (4)$$

Figure 3 shows how each vertical column is divided into three regions:

- The CO₂ plume between Z and $Z + h$ with residual brine saturation $s_{w,r}$, CO₂ saturation $1 - s_{w,r}$, and CO₂ mobility $\lambda_{n,e} = \lambda_n(1 - s_{w,r})$.
- The residual region between h and h_{\max} with CO₂ saturation $s_{n,r}$, brine saturation $1 - s_{n,r}$, and brine mobility $\lambda_{w,e} = \lambda_w(1 - s_{n,r})$.
- The region below h_{\max} filled by brine.

We hence define vertically-averaged quantities:

$$\mathbf{K} = \frac{1}{H} \int_Z^{Z+H} \mathbf{k}_\parallel d\zeta, \quad (5)$$

$$\mathbf{\Lambda}_n(h) = \frac{1}{H} \left[\int_Z^{Z+h} \lambda_{n,e} \mathbf{k}_\parallel d\zeta \right] \mathbf{K}^{-1} \quad (6)$$

$$\begin{aligned} \mathbf{\Lambda}_w(h, h_{\max}) &= \frac{1}{H} \left[\int_{Z+h}^{Z+h_{\max}} \lambda_{w,e} \mathbf{k}_\parallel d\zeta \right. \\ &\quad \left. + \int_{Z+h_{\max}}^{Z+H} \lambda_w(1) \mathbf{k}_\parallel d\zeta \right] \mathbf{K}^{-1} \end{aligned} \quad (7)$$

Combining these expressions with Darcy's law (2) and setting $\Delta\rho = \rho_w - \rho_n$, we obtain vertically-integrated fluxes:

$$\vec{V}_n = -H \mathbf{\Lambda}_n \mathbf{K} [\nabla_\parallel (P_Z - \rho_n g_\zeta Z) - \rho_n \vec{g}_\parallel], \quad (8)$$

$$\vec{V}_w = -H \mathbf{\Lambda}_w \mathbf{K} [\nabla_\parallel (P_Z - \rho_w g_\zeta Z) - g_\zeta \Delta\rho \nabla_\parallel h - \rho_w \vec{g}_\parallel]. \quad (9)$$

To develop the usual fractional-flow formulation, we introduce total velocity $\vec{V} = \vec{V}_n + \vec{V}_w$, assume that \mathbf{K} and $\mathbf{\Lambda}_\alpha$ commute (\mathbf{K} isotropic or \mathbf{k}_\parallel constant in ζ), and sum (3) over phases. After some manipulations, we obtain a pressure equation:

$$\begin{aligned} \nabla_\parallel \cdot \vec{V} &= Q, \\ \vec{V} &= -H \mathbf{\Lambda} \mathbf{K} [\nabla_\parallel P_z \\ &\quad - (\rho_n \mathbf{F}_n + \rho_w \mathbf{F}_w) (\vec{g}_\parallel + g_\zeta \nabla_\parallel Z) - \mathbf{F}_w g_\zeta \Delta\rho \nabla_\parallel h], \end{aligned} \quad (10)$$

where $\Lambda(h, h_{\max}) = \Lambda_w(h, h_{\max}) + \Lambda_n(h)$ and $\mathbf{F}_\alpha(h, h_{\max}) = \Lambda_\alpha \Lambda^{-1}$, and a transport equation:

$$\frac{\partial}{\partial t} \Phi + \nabla_{\parallel} \left[\mathbf{F}_n \vec{V} + \Delta \rho \mathbf{K} \Lambda_w \mathbf{F}_n [\vec{g}_{\parallel} + g_{\zeta} \nabla_{\parallel} (Z + h)] \right] = Q_n, \quad (11)$$

where $\Phi(h, \xi, \eta) = \int_Z^{Z+h} \phi(1 - s_{w,r}) d\zeta$ and $Q_n = \int_Z^{Z+h} q_n d\zeta$. This is the so-called h -formulation of the VE model. If ϕ and \mathbf{K} are constant in the ζ -direction, we get the following upscaled porosity and relative mobilities:

$$\begin{aligned} \Phi(h) &= \phi(1 - s_{w,r})h + \phi s_{n,r}(h_{\max} - h), \\ \Lambda_n(h) &= h\lambda_{n,e}, \\ \Lambda_w(h, h_{\max}) &= (h_{\max} - h)\lambda_{w,e} + (H - h_{\max})\lambda_w(1). \end{aligned}$$

To simplify implementation and avoid having to treat the curvilinear grid explicitly, we express the transport equation in terms of global coordinates by writing $\vec{g}_{\parallel} + g_{\zeta} \nabla_{\parallel} (Z + h) = |g| \nabla_{\parallel} z_n$, where z_n is the true vertical position of the CO₂-brine interface, and approximating ∇_{\parallel} by ∇_{xy} to obtain:

$$\frac{\partial}{\partial t} \Phi(h, x, y) + \nabla_{xy} \left[\mathbf{F}_n \vec{V} + \Delta \rho \mathbf{K} \Lambda_w \mathbf{F}_n [|g| \nabla_{xy} (Z + h)] \right] = Q_n. \quad (12)$$

As an additional approximation, we consider h to be measured along \vec{e}_z . Errors associated with the transformation of the grid and the transport equation are discussed in more detail in Appendix A.

In the absence of viscous forces, the stationary state of the system is given by the balance between gravity and the ‘‘capillary pressure’’ $\nabla_{xy} h$. Writing the transport equation in physical coordinates honors explicitly the condition from the underlying 3D model that a horizontal interface is a stationary state.

Example 1. Consider a simple 1D model with a sealing caprock given by

$$z_t = D - L_1 \sin\left(\frac{x}{L_1}\right) \tan \theta + A \sin\left(\frac{2\pi x}{L_2}\right), \quad (13)$$

where D is maximum depth, $\theta = 0.03$ is the initial tilt angle, $L_1 = 20$ km is the characteristic length of the antiform structure, and $L_2 = 0.3$ km is the wave-length L_2 of the small-scale structures; see Figure 4. For the amplitude, we use either $A = 0$ or $A = 2$ m. The density of CO₂ is assumed to follow a model taken from [51] with a temperature variation given by

$$T = zK_T + T_s, \quad K_T = 30\text{K/km}, \quad T_s = 286\text{K}. \quad (14)$$

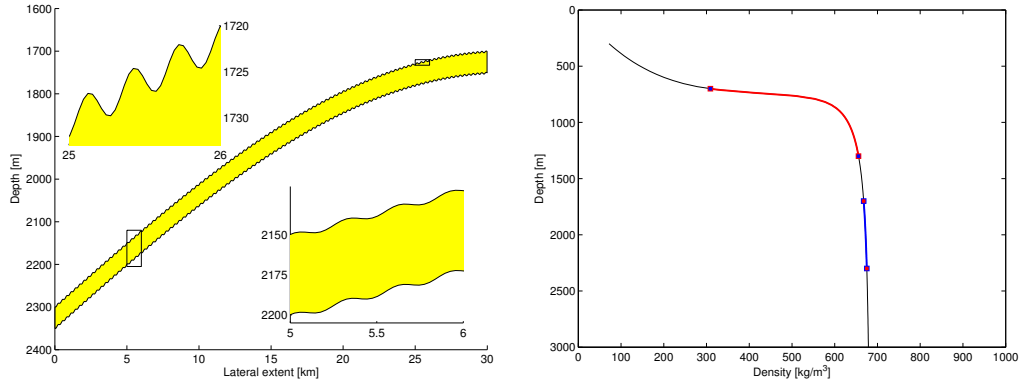


Figure 4: *Left:* the geometry of Example 1. *Right:* the density of CO_2 given hydrostatic pressure; the blue line represents a deep model with $D = 2300$ m and the red line corresponds to a model with $D = 1300$. (From `showAquiferModel.m` and `showDensityVariation.m`.)

Given a hydrostatic pressure computed from a constant brine density of 1100 kg/m^3 , there will be different regimes of density variation depending on the depth of the aquifer as shown in Figure 4. Here, we set $D = 2300$ m, at which the variation in density is relatively small. (The temperature varies from 335 to 357 K.) In all calculations, we use isotropic permeability of 1 Darcy and constant porosity of 0.2. The brine and rock volumes are considered to be linear functions of pressure, with respective coefficients $4.3 \cdot 10^{-5} \text{ bar}^{-1}$ and $1.0 \cdot 10^{-5} \text{ bar}^{-1}$, based on a reference pressure of 100 bar. The storage scenario consists of fifty years of injection at an annual rate of $760 \cdot 10^6 \text{ kg/year}$. The model is discretized with 1000 uniform grid cells, and we use uniform time steps of two years during the injection period and twenty years during the subsequent 2000 year migration period.

In its simplest form, the VE model describes a plume that continues to migrate upward until it either reaches the top of the formation, or until all of the CO_2 has become trapped in geometric structures in the caprock. If nonzero residual saturation is introduced, the migrating plume will leave behind a trail of residually trapped CO_2 . As a result, the tail of the plume will move faster than the tip, which means that CO_2 injected into an infinite aquifer without structural traps will only spread a finite distance, see [52]. The left plot of Figure 5 compares plume thickness computed with and without residual trapping after 700 years. The presence of small-scale variation (rugosity) in the top seal will generally lead to trapping of small

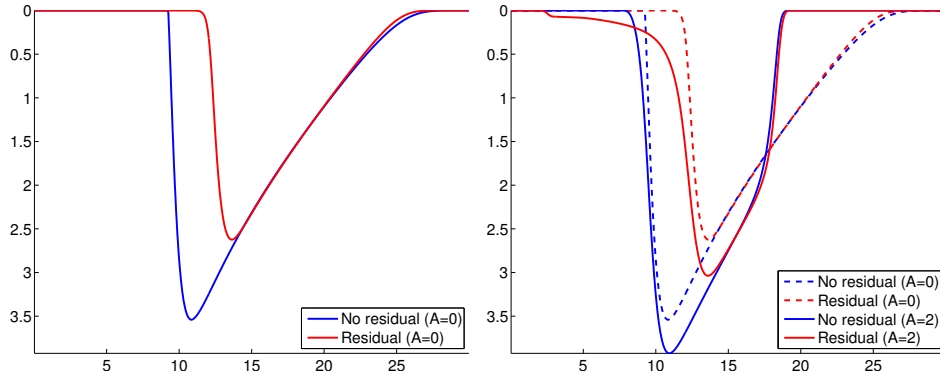


Figure 5: Thickness of the CO_2 plume simulated by sharp-interface models for the 1D sloping aquifer in Example 1 after approximately 700 years. The left plot shows the effect of extending the basic model (blue line) with residual trapping (red line) for a surface without small-scale structures. In the right plot, these two outcomes (shown as dashed lines) are compared with calculations that also include small-scale undulations; in the plot, the solutions are averaged over a region that is larger than the small-scale undulations. (From `residualExample.m`.)

Table 1: Computational cost for the simulations in for Example 1 observed using MRST 2015a with MATLAB R2014a on an Intel Xeon 3.47GHz CPU.

| | no residual | residual |
|-----------------------|-------------|----------|
| Smooth caprock | 42 sec | 63 sec |
| Caprock with rugosity | 64 sec | 172 sec |

amounts of CO_2 , thereby retarding the migration of the plume [33]. This, in turn, changes the solution to also include a shock at the front of the plume, as seen in the left plot of Figure 5 and in more detail for the case with no residual trapping in Figure 6. In Section 4.1, we will develop effective relative-permeability models that capture the retardation effect caused by caprock rugosity.

The four simulations were performed using a general-purpose, fully-implicit black-oil solver from MRST [12]; more details will be given in the next section. Computational costs are reported in Table 1. With residual trapping and rugosity, the prescribed 20-year time step is straddling the stability limit and hence the nonlinear solver was forced to halve many of the time steps, which explains the significant increase in CPU time. On the other hand, the relatively high computational cost is a MATLAB artifact that poorly reflects the efficiency of the underlying algorithm: With only 1000 cells in the model,

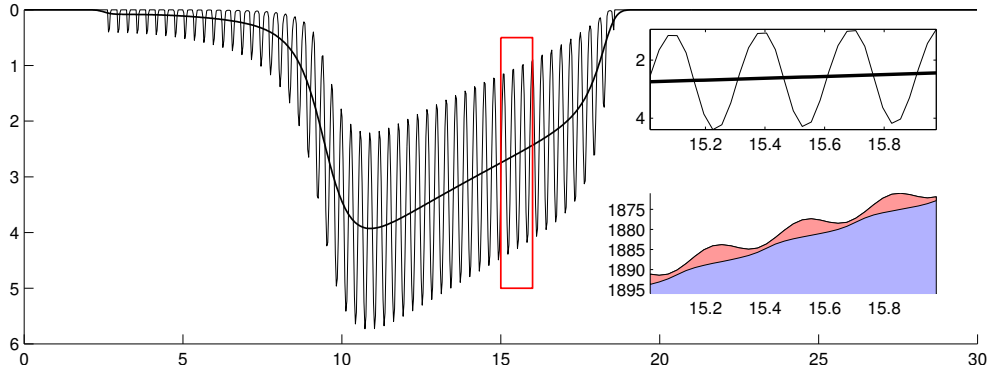


Figure 6: Sharp-interface simulation of the 1D aquifer with small-scale undulations in the top surface. The thin oscillatory black line is the thickness of the CO_2 plume after approximately 700 years and the thick line is the average. The upper inset shows a magnification of the red square, while the lower inset shows the corresponding vertical fluid distribution in the real coordinate system. (From `residualExample.m`.)

the computational overhead induced by the combination of MATLAB and automatic differentiation is significant. In these particular runs, only 3% of the total CPU time was spent solving linear systems. This is a known issue with MRST, which is significantly diminished if one goes to models with more unknowns.

Finally, we compare the simulation outcome of the VE model with that of a full 3D model for the case with smooth caprock ($A = 0$). The 3D model has a vertical resolution of 30 cells, with progressively thinner cells towards the top of the aquifer to better resolve the shape of the plume. The lateral resolution is 200 cells for both models. We use linear relative permeabilities and zero capillary pressure. As we can see from the left plot in Figure 7, there is an almost perfect match between the models without residual saturation, except that plume in the 3D simulation has a characteristic staircase shape that will be present in all 3D simulations unless the width of the capillary fringe exceeds the height of the grid blocks. When residual saturation is included, the match between models still remains close. The required computational times to simulate 2000 years of migration using our laptop (Core i7-4500U processor, 8 GB RAM) for the VE simulations without/with residual saturations were 64 and 66 seconds, respectively. For the corresponding 3D simulations, the runtimes were 673 and 1005 seconds. We emphasize, however, that neither the VE nor the 3D simulation codes have been optimized for speed.

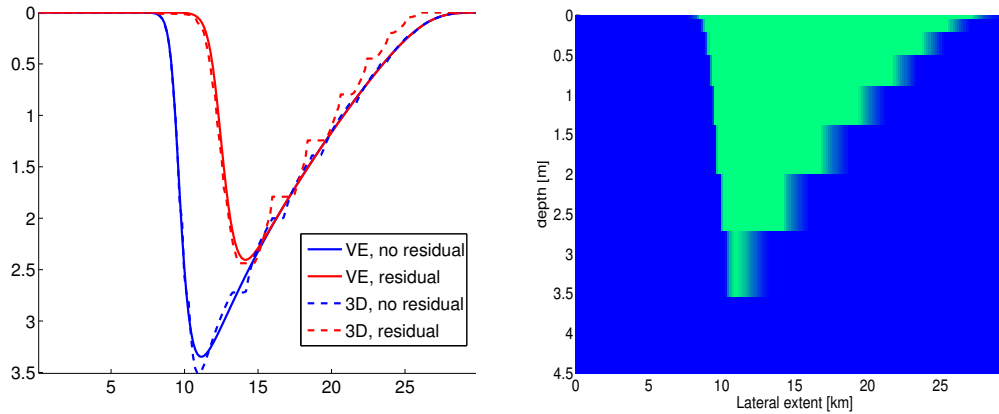


Figure 7: Comparison between the VE models and corresponding full 3D models for the 1D sloping aquifer in Example 1 after approximately 700 years. The left plot compares the plume thicknesses resulting from VE and 3D simulations with (red) and without (blue) residual trapping included. The right plot illustrates the upper 4.5 meters of the aquifer 3D model (flattened, for presentational clarity) and the CO_2 saturation after approximately 700 years for the case without residual trapping. The complete phase segregation is evident, and we also see how the vertical grid discretization is related to the 'staircase' shaped curves shown on the left plot.

The simple aquifer geometry introduced above will be used repeatedly throughout the paper as a means to illustrate and discuss how including additional physical mechanisms affects the plume migration. In the next example, we consider a scenario with a touch of more geological realism.

Example 2. *The Pliocenesand model from the CO_2 Storage Atlas [53] consists of 13 484 active cells and describes a ridge ending in a large plain. The actual sand body lies too shallow to be a candidate for CO_2 storage, but the model can be used as a test case if we increase its burial depth to, e.g., a thousand meters. The top surface has almost no fine-scale structure and thus allows for a very low percentage (0.02%) of structural trapping compared to the overall volume of the whole sand body. To store CO_2 , one should therefore primarily consider residual and solubility trapping. We set the pressure to 100 bar at the top point and assume a homogeneous porosity of 25% and a homogeneous, isotropic permeability of 1200 mD. Ten mega-tonnes of CO_2 are injected annually for fifty years from a single injection point halfway down the slope. Brine has constant density 975.86 kg/m^3 , viscosity 0.3086 cP , residual saturation equal 0.1, and an end-point mobility of 0.2142. The*

CO₂ phase has constant density 686.54 kg/m³, viscosity 0.056641 cP, residual saturation 0.2, and an end-point mobility of 0.85. In the simulation, we use time steps of two years during injection and ten years afterward.

The injected CO₂ plume moves upward towards the plain, leaving behind a trail of residually trapped CO₂. Figure 8 shows the CO₂ plume at the end of injection and after one hundred years along with an instantaneous volumetric inventory. From the pie chart, we see that 6% of the injected CO₂ has been residually trapped after 100 years, while the remaining volume is still inside the plume. However, a significant fraction of the plume volume (20% of the injected volume) will eventually remain as residually trapped when the plume leaves its current position.

After 500–600 years, the tip of the plume has crossed the upper plain and reached the open boundary. The amount that leaks will roughly be proportional to the square of the plume thickness. Since the tip of the plume is very thin and the caprock is almost horizontal, the leakage is insignificant at first and only visually noticeable in the CO₂ inventory in Figure 9 after another 200–300 years. At the end of simulation, only 3% has left our computational domain and the mobile CO₂ has reached a region with a very low sloping angle and is thus almost immobilized.

Figure 10 reports CPU time per step in a sequentially implicit simulator that utilizes a standard two-point pressure solver and a fully-implicit transport solver from the `incomp` module of MRST [10] and a fully-implicit black-oil solver based on automatic differentiation [12]. Both simulators have time-step control and will, if necessary, reduce the time steps to ensure convergence. During the injection period, the flow is dominated by the 'advective' $\mathbf{F}_n \vec{V}$ term in (12) resulting from heightened pressure in the near-well region and the sequentially implicit solver is significantly more efficient, partially because of the significant overhead in the black-oil solver as discussed in Example 1. During the first 600 years after injection ceases, the migration is dominated by the hyperbolic $\nabla_{xy}Z$ term in (12), and the two simulators are equally efficient. After this point, the parabolic $\nabla_{xy}h$ term, which here plays the role of capillary forces in a conventional flow model, gradually becomes more important. The influence of the parabolic transport terms is more difficult to resolve in a sequential formulation and hence we see a gradual increase in the CPU time of each transport step. After 1260–1280 years, most of the mobile plume has reached the flat plane and the plume is approaching a steady state. The dynamics of this state is governed mainly by the coupling of the gravitational $\nabla_{xy}Z$ and the parabolic $\nabla_{xy}h$ term and

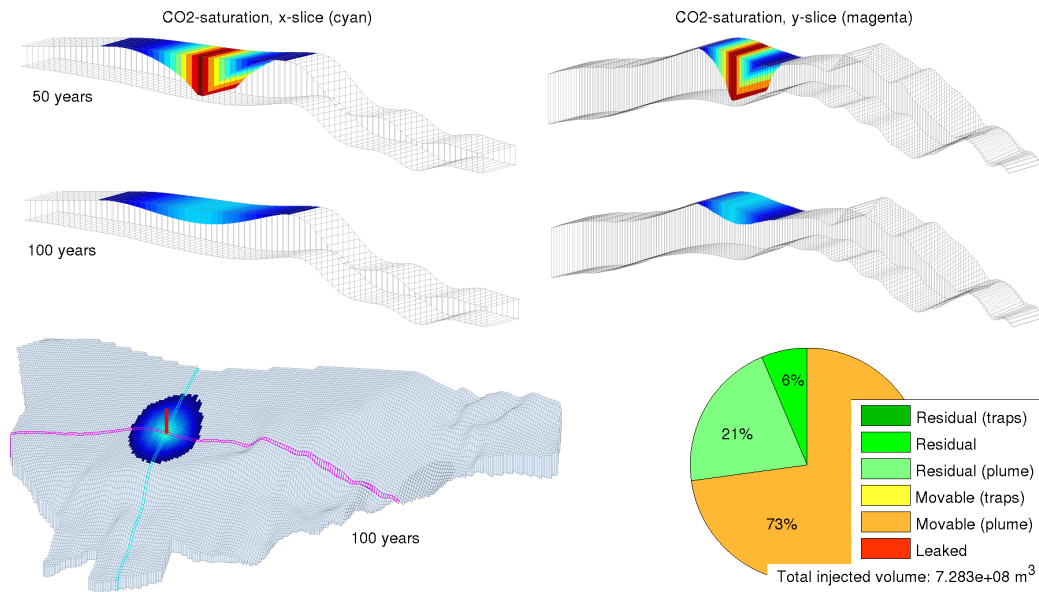


Figure 8: Injection into the Pliocenesand aquifer from a single injection point. The plots show fluid distribution at the end of the injection and after 50 years of migration, as well as an inventory of the trapping observed after 100 years. (From `firstPlioExample.m`.)

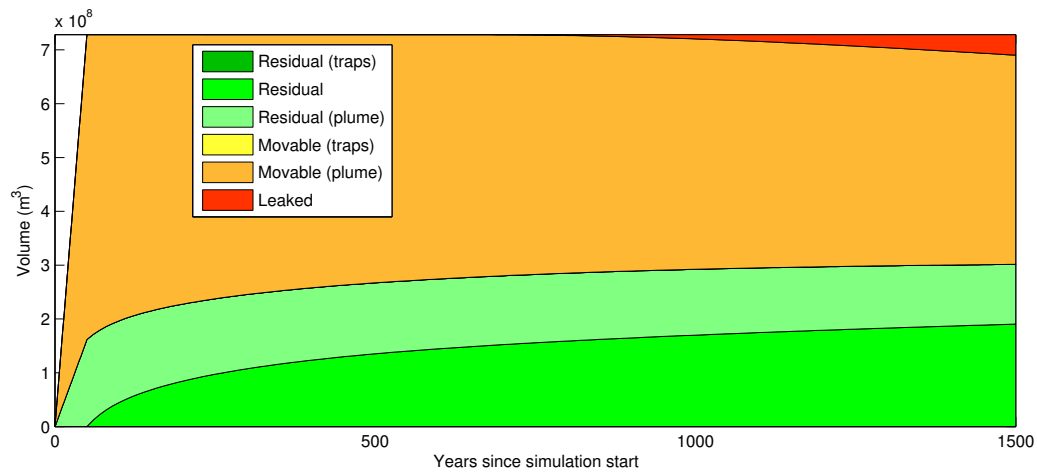


Figure 9: Detailed inventory of the CO₂ trapping process in the Pliocenesand formation over a period of 1500 years. (From `firstPlioExample.m`.)

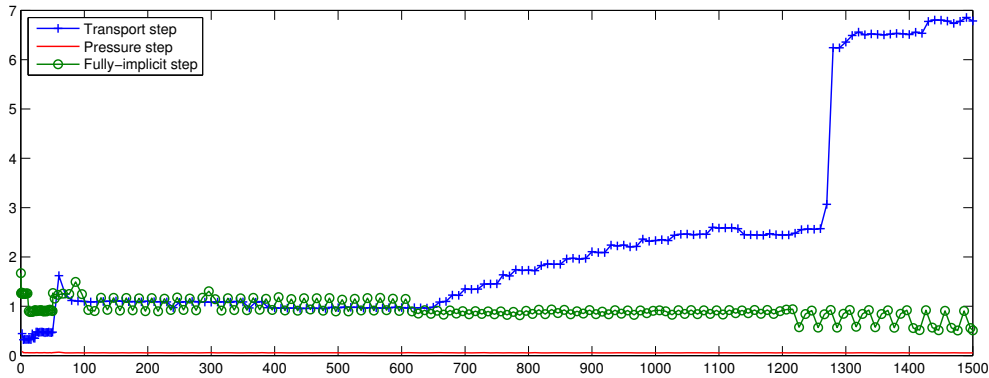


Figure 10: CPU times in seconds for each step in a sequentially implicit simulation and in a fully-implicit, black-oil type simulation of the Pliocenesand injection measured for MRST 2015a with MATLAB R2014a on an Intel Xeon 3.47GHz CPU.

the effects of these terms in the pressure equation. These forces seek to enforce a flat interface between the CO_2 plume and the underlying brine. Operator-splitting methods, and in particular methods based on a total velocity formulation, are not suited for cases with such strong coupling between pressure and transport. In our case, the transport solver has to aggressively cut the time steps, which results in a dramatic increase in the CPU time. The fully-implicit formulation, on the other hand, is robust with respect to changing force balances and can, in particular, accurately resolve the near steady-state towards the end of the simulation.

As an alternative to using h as the primary unknown, one can use the fractional content $S = h/H$ of CO_2 in the vertical column to derive the so-called S -formulation having equations that look like standard pressure and transport equations known from the petroleum literature with S playing the role of saturation. In the rest of the section, we will detail the derivation for vertically homogeneous rock properties ϕ and \mathbf{k} . By integration over the column, it is easy to show that:

$$\begin{aligned}
 S(h, h_{\max}) &= \frac{h(1 - s_{w,r}) + (h_{\max} - h)s_{n,r}}{H}, \\
 S_{\max}(h_{\max}) &= \frac{h_{\max}(1 - s_{w,r})}{H}.
 \end{aligned}
 \tag{15}$$

where we recall that $s_{w,r}$ and $s_{n,r}$ are constants. Inversely, h can be written

in terms of S and S_{\max} :

$$\begin{aligned} h(S, S_{\max}) &= H \frac{S(1 - s_{w,r}) - S_{\max}s_{n,r}}{(1 - s_{w,r})(1 - s_{w,r} - s_{n,r})}, \\ h_{\max}(S_{\max}) &= \frac{HS_{\max}}{1 - s_{w,r}}. \end{aligned} \tag{16}$$

To obtain a set of standard transport equations formulated in S , we transform our coordinate system so that $Z \equiv 0$ and then write:

$$\begin{aligned} \Lambda_n(S, S_{\max}) &= \frac{1}{H} \left[\int_0^h \lambda_{n,e} \mathbf{k}_{\parallel} d\zeta \right] \mathbf{K}^{-1} = \frac{h(S, S_{\max})}{H} \lambda_{n,e} \\ \Lambda_w(S, S_{\max}) &= \frac{1}{H} \left[\int_h^{h_{\max}} \lambda_{w,e} \mathbf{k}_{\parallel} d\zeta + \int_{h_{\max}}^H \lambda_w(1) \mathbf{k}_{\parallel} d\zeta \right] \mathbf{K}^{-1} \\ &= \frac{h_{\max}(S_{\max}) - h(S, S_{\max})}{H} \lambda_{w,e} + \frac{H - h_{\max}(S_{\max})}{H} \lambda_w(1) \end{aligned}$$

where the last equality sign in each equation assumes vertically constant rock properties. This formulation is easy to implement in a standard reservoir simulator; all one has to do is to replace the evaluation of mobility and capillary pressure functions by special functions that compute vertically integrated quantities. Likewise, the S -formulation is a more natural starting point when extending the vertical equilibrium model to black-oil type models or including physical effects like compressibility and hysteresis. A more detailed discussion of hysteresis is given in [50].

4. Extending with more flow physics

In this section, we present a general formulation that includes residual trapping, compressibility, dissolution and resulting hysteresis effects. Apart from capillary fringe, which is discussed in [50], our models incorporate the physical effects discussed by Gasda et al. [30], but the formulation and notation will follow that of standard black-oil models used in the petroleum industry (see Appendix B) to make similarities and differences with models implemented in standard simulators as clear as possible.

The effects discussed in this section can be divided in two categories. The first category consists of capillary and hysteretic effects, which change effective mobilities and capillary pressures, and whose upscaled effect can be derived from considering one vertical column at a time. In Example 1 we also

saw how small amounts of CO₂ trapped inside small-scale undulations in the top surface may retard the plume migration, which will in turn lead to hysteretic effects and changes in the effective mobility. Retardation phenomena of this form can therefore also be included in the first category. The second category includes compressibility, which affects the form of the mass balance equations, and dissolution that also changes the number of unknowns and equations.

4.1. Sub-scale caprock variations

In potential CO₂ storage sites, the top surface that separates the permeable aquifer from the overlying caprock will have natural variability that spans several length scales. Whereas the characteristic dip angle caused by regional uplift may be constant for hundreds of kilometers, the topography on a kilometer scale will be more varied and contain different types of antiform structures (domes, anticlines, traps, etc) that can be identified from seismic surveys. In [33] it was demonstrated that various kinds of roughness straddling the scale of seismic resolution will impact the plume and potentially cause significant retardation in its updip migration. On an even smaller scale, the top surface is characterized by submeter fluctuations that can only be observed in outcrop studies. Effective models that capture sub-scale roughness and rugosity effects [34, 35] are generally needed to study realistic migration scenarios, because even though VE models are highly efficient, they cannot resolve all relevant structural features in large-scale formations. Here, we briefly review such effective models based on analytical and numerical up-scaling techniques for the case without residual trapping in 1D. Figure 11 shows a schematic of our conceptual setup.

In the simplest approach to upscaling, we assume that caprock undulations create a volume in which CO₂ becomes trapped and cannot flow. This volume is represented as a layer of zero horizontal permeability (accretion layer), whose thickness is constant over the averaging length $h_a = \frac{1}{L} \int_0^L h_t(x) dx$, see Figure 11 for notation. Introducing the accretion layer reduces the effective height that is accessible to fluid flow to $H_e = \bar{H} - h_a$, where \bar{H} is the mean aquifer thickness over the length scale L . This model cannot distinguish the effect of different caprock topographies that give the same trapped volumes.

To capture the effect of sub-scale undulations more accurately, we average the depth-integrated rock and rock-fluid properties in the horizontal

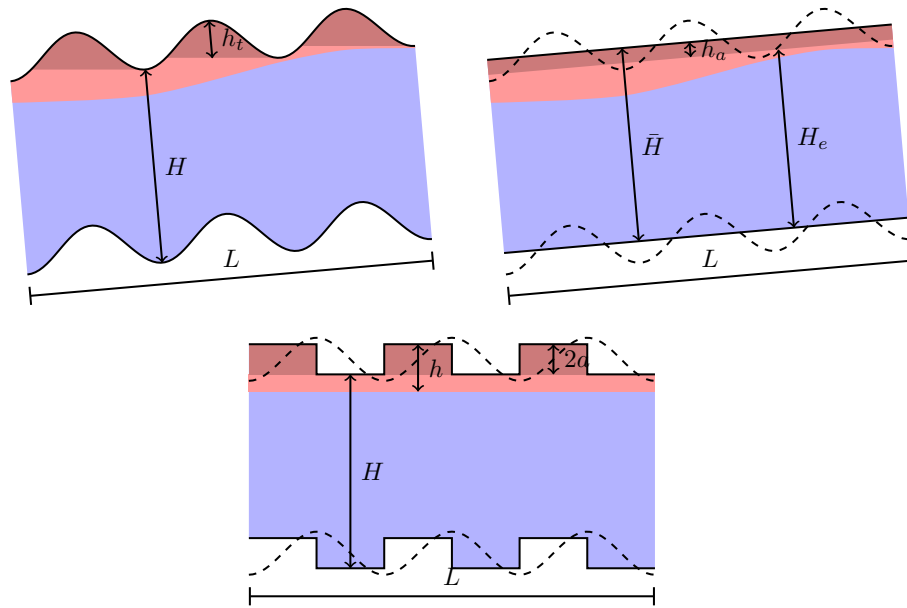


Figure 11: Upscaling of small-scale caprock undulations. *Upper left:* the representative volume to upscaled, where h_t is the height of the CO_2 column inside the sub-scale traps. *Upper right:* the sub-scale undulations have been replaced by a flat accretion layer inside which CO_2 is immobile, giving an aquifer with a reduced effective height H_e . *Lower:* sub-scale undulations are assumed to be step functions of amplitude a and the dip angle is disregarded to simplify the analytic calculation of upscaled relative permeability.

direction. For permeability, we use a simple homogeneous-equation approach for a periodic medium [55], resulting in an effective permeability $\bar{K} = [(\bar{H}/L) \int_0^L (KH)^{-1} dx]^{-1}$. For the relative mobilities, we use a steady-state method that assumes periodicity in the lateral direction (inflow across the left boundary equals outflow across the right boundary) and computes average relative permeabilities as function of volume-averaged saturations values \bar{S} . We start by observing that the total velocity is zero after injection has ceased. To obtain a steady-state solution that corresponds to a given average saturation \bar{S}^i inside our averaging volume, we can therefore solve

$$\phi \partial_t s^i + \nabla \left[\mathbf{k} \frac{\lambda_w \lambda_n}{\lambda_w + \lambda_n} (\Delta \rho \vec{g} + \nabla p_c) \right] = 0, \quad s^i(\vec{x}, 0) = \bar{S}^i, \quad (17)$$

until steady state subject to periodic conditions in the x -direction and no flow across the top and bottom surfaces. For each steady-state solution $s^i(\vec{x})$, we reconstruct phase pressures from

$$\nabla \bar{v}_\alpha^i = 0, \quad \bar{v}_\alpha^i = -\mathbf{k} \lambda_\alpha(s_\alpha^i) \nabla [p_\alpha^i - \rho_\alpha \vec{g}] \quad (18)$$

subject to a pressure drop Δp in the x -direction and no flow across the top and bottom surfaces. This gives averaged phase fluxes F_α , which can be combined with the upscaled Darcy's law for each phase, $F_\alpha = -\bar{H} \bar{K} \bar{\Lambda}_\alpha \Delta p / L$, to derive values for $\bar{\Lambda}_\alpha$. By repeating this procedure for an increasing sequence of saturation values, we can compute a set of averaged mobilities $\bar{\Lambda}_\alpha$ as function of \bar{S} or an equivalent average plume height \bar{h} .

Analytical expressions can be defined if we make further simplifying assumptions [34]. First, we can approximate the fine-scale undulations by a geometric form defined relative to a top surface that is flat on the averaging scale; see the lower plot in Figure 11. With a sharp interface assumption, it then follows that

$$\begin{aligned} \bar{\Lambda}_n &= \left[\frac{\bar{H} \bar{K}}{L} \int_0^L \frac{1}{h K \lambda_{n,e}} dx \right]^{-1}, \\ \bar{\Lambda}_w &= \left[\frac{\bar{H} \bar{K}}{L} \int_0^L \frac{1}{(H-h) K \lambda_w(1)} dx \right]^{-1}. \end{aligned} \quad (19)$$

Second, for small pressure gradients and an averaging scale much smaller than the total domain, we assume that the CO₂-brine interface is flat on the fine scale so that $h(x)$ is a simple function of the function describing the

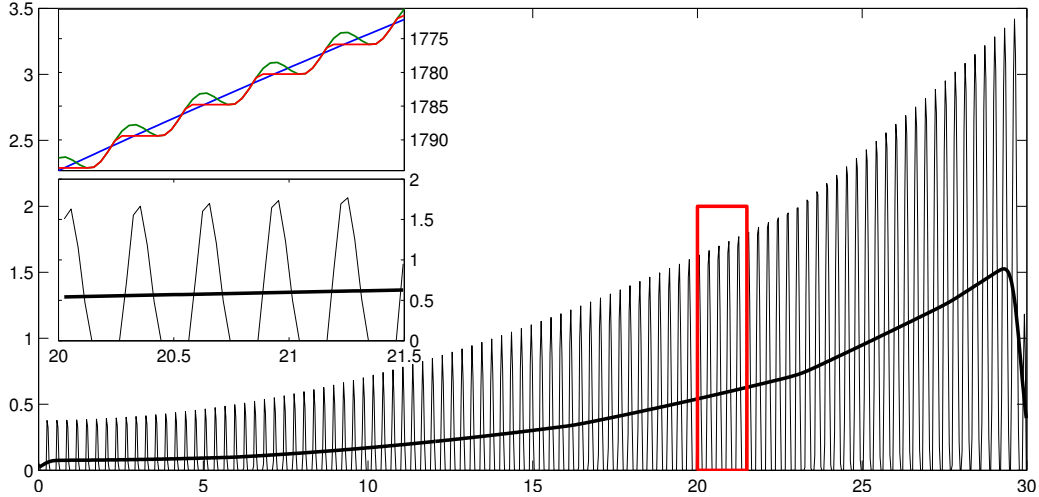


Figure 12: Estimation of the parameter characterizing sub-scale undulations. The thin line is the local trap height $h_t(x)$ and the thick line is the averaged height $a(x)$. The lower inlet shows a zoom of $h_t(x)$ and $a(x)$ inside the red square. The upper inlet zooms in on the top surface (green), the spill-point level of the local traps (red), and the top surface for the model without small-scale undulations (blue). (From `upscaleRelPerms.m` and `showUpscaledRelperms.m`.)

surface topography and (19) can be computed analytically. From the form of (19) we also see that $\bar{\Lambda}_n = 0$ if $h(x) = 0$ at some point, and hence CO_2 will only be able to flow if the interface with brine lies deeper than the lowest point in the local topography.

Example 3. *To compare the simple accretion layer model with effective models obtained by assuming sinusoidal or square undulations, we revisit the 1D aquifer from Example 1. In the true model, we set $A = 2$ and use the different upscaled relative permeabilities to compute approximate solutions for the model geometry without undulations ($A = 0$). Because the large-scale structure of the aquifer is the left half of an antiform, the thickness of the CO_2 layer that will be trapped inside small-scale undulations can simply be computed as $h_t(x) = \max_{r \geq x} z_t(r) - z_t(x)$. Then, the resulting function $h_t(x)$ is averaged over a length scale $L \gg L_2$ to obtain*

$$a(x) = \left[\int_{-L/2}^{L/2} h_t(x+r)w(r) dr \right] / \left[\int_{-L/2}^{L/2} w(r) dr \right],$$

where w is a standard Gaussian mollifier function. Figure 12 illustrates the different steps of this estimation process.

Figure 13 compares the true plume depth with approximate solutions obtained by the accretion-layer model and the two analytical approaches. One might have expected that the model based on sinusoidal substructure would be closest to the fine-scale simulation, but by a coincidence, the simple accretion-layer model is most accurate. The plot to the right in Figure 13 compares the relative permeabilities of the three effective models with the numerically upscaled relative permeability sampled at three different dip angles $\theta = 0, 0.0162,$ and 0.03 that correspond to the angle at the top, midway and at the deepest point of the actual formation, respectively. The plot shows that when the height of the tip of the plume is in the range 2–4, the relative permeability of the accretion-layer model is much closer to those of the numerically upscaled models, and this model will therefore give the best match for the front shock speed. The accretion curve is significantly different from the numerically upscaled curves for $\theta < 0.03$, and hence this model cannot be expected to provide a good approximation towards the top of the antiform. We also note that whereas the trailing rarefaction wave seen in the fine-scale solution can be explained by the convex shape of the numerically upscaled relative permeability, it cannot be predicted by the concave curves of the ‘sinus’ and ‘square’ effective models. Better coarse-scale simulation can be obtained by introducing effective models that depend on both the local trapping volume and the local dip angle. In 2D, this would immediately involve tensorial relative-permeability effects.

4.2. Compressibility and dissolution

In this section, we extend the basic VE model to compressible flow including dissolution of CO_2 into brine and write the resulting model as a set of two-dimensional, two-phase, black-oil equations. We start by writing the upscaled Darcy’s law for each phase as,

$$\begin{aligned}\vec{v}_w &= -\lambda_w(p_w, s_w, s_{\max})[\nabla p_w - g\rho_w(p_w, c)\nabla Z], \\ \vec{v}_n &= -\lambda_{rn}(p_n, s_n, s_{\max})[\nabla p_n - g\rho_n(p_n)\nabla Z].\end{aligned}\tag{20}$$

Here, lower-case symbols have been used to emphasis the similarity with the standard black-oil model and will henceforth represent upscaled quantities unless specified otherwise. The water phase is assumed to consist of brine containing a concentration c of dissolved CO_2 , while hysteretic effects are

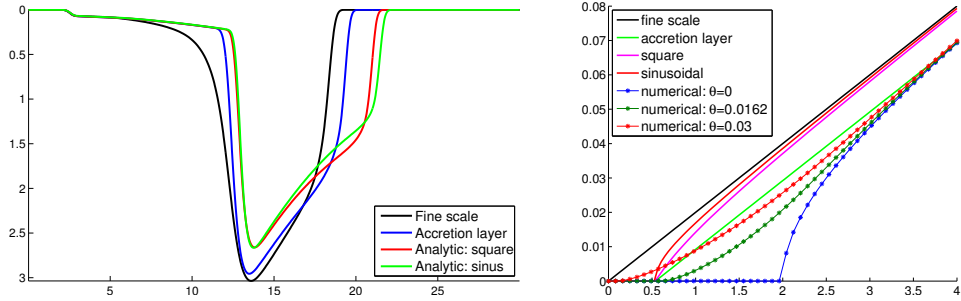


Figure 13: Upscaling of sub-scale caprock topography. *Left:* The fine-scale solution compared with approximate solutions computed using an accretion-layer model and two analytical models that assume sinusoidal and square sub-scale undulations, respectively. *Right:* The corresponding upscaled relative permeabilities shown as functions of h and sampled at $x = 20$ km. In addition, lines with markers show effective relative permeabilities obtained by direct numerical upscaling of the 1D aquifer model for three different dip angles θ . (From `upscalingExample.m` and `showUpscaleRelPerms.m`.)

modeled by tracking the maximal saturation s_{\max} , as defined in (15). The viscosities, relative permeabilities, and densities all depend on pressure, but are assumed to be constant within the vertical column of the underlying 3D model. Unlike in Section 3, we now operate with distinct phase pressures p_α , which are evaluated at the top surface. In other words, p_α refers to pressures defined in cells of the 2D surface grid that follows the caprock topography and should not be confused with pressures inside cells of a 3D volumetric model. If $p_{\alpha,i}$ represents the fine-scale phase pressures at the CO_2 -brine interface, it follows by assuming hydrostatic conditions that

$$\begin{aligned}
 p_w &= p_{w,i} - g\rho_w h, \\
 p_n &= p_{n,i} - g\rho_n h, \\
 p_c &= p_n - p_w = p_e + g\Delta\rho h
 \end{aligned}
 \tag{21}$$

Here, $p_e = p_{n,i} - p_{w,i}$ is the fine-scale entry pressure, whereas p_c can be understood as an upscaled “capillary pressure”. Because h can be obtained from the upscaled saturation by (16), the relation between the phase pressures can be written as a function of saturation and pressure:

$$p_w = p_n - p_c(p, s_n, s_{\max})
 \tag{22}$$

In a standard black-oil model, p_c is usually a function of s_n and s_{\max} only. To evaluate densities, we introduce the (reciprocal) formation-volume factors

b_α for each phase, which relate the densities at reservoir conditions to the densities $\rho_{\alpha,s}$ at surface conditions

$$\begin{aligned}\rho_w(p, c) &= (\rho_{w,s} + c\rho_{n,s})b_w(p, c), \\ \rho_n(p) &= \rho_{n,s}b_n(p).\end{aligned}\tag{23}$$

Next, the conservation of CO₂, water, and dissolved CO₂ is written as

$$\begin{aligned}\frac{\partial}{\partial t} [\phi b_n s_n + \phi c b_w (1 - s_n)] + \nabla \cdot [b_n \vec{v}_n + c b_w \vec{v}_w] &= q_n, \\ \frac{\partial}{\partial t} [\phi b_w (1 - s_n)] + \nabla \cdot (b_w \vec{v}_w) &= q_w, \\ \frac{\partial}{\partial t} [\phi c b_w (1 - s_n)] + \nabla \cdot (c b_w \vec{v}_w) &= q_{n,\text{dis}}.\end{aligned}\tag{24}$$

The effect of dissolution on long-term CO₂ storage has been widely discussed, and in particular, the possibility of enhanced dissolution because of convective mixing [56, 57, 58]. For an overview of this topic see [59]. The studies are predominantly theoretical and carried out for homogeneous systems or idealized heterogeneous cases, see [60]. For real cases, the only data on dissolution rates is an estimated upper limit of 1.8% per year for the Sleipner injection [61]. This estimate is consistent with a later study based on inversion of gravimetric data [62]. For convective mixing in porous media, one can only find indirect evidence of dissolution for analogous problems like salt dissolution, [63, 64]. Even for convection of heat, the few conclusive measurements are of convection induced purely by heating from below, see [65, 66] for reviews.

Despite the uncertainty that surrounds dissolution, we have included this effect in our models to be able to illustrate how dissolution may potentially affect the long-term fate of injected CO₂. For a standard black-oil type of equation, the dissolution of gas is assumed to be instantaneous as long as the fluid phase is undersaturated. That is, the concentration c corresponds to the solution gas/oil ratio r_s used for petroleum systems. To mimic this type of model, we drop the last conservation law in (24) and set $c = c_{\text{max}}$ and $s_{\text{max}}(t) = \max_{\tau \leq t} s_n(\tau)$ wherever $s_n > 0$. We refer to this as the *instantaneous dissolution model*. Compared with the general black-oil formulation in Appendix B, this would be a model in which brine is given the role of the oleic phase and the supercritical CO₂ is given the role of the gaseous phase.

More accurate modeling of dissolution will introduce two main changes compared with traditional black-oil models: (i) dissolution is rate limited,

and (ii) dissolution affects the hysteresis variable², i.e., s_{\max} or h_{\max} which tracks the maximum height at which CO_2 exists. The CO_2 will dissolve into brine from the layer of residual CO_2 saturation that separates the brine phase from the free CO_2 plume, or directly from the plume when no such layer is present (i.e., when $s_{\max} = s_n$). In `MRST-co2lab`, the corresponding dissolution rate is modeled as

$$q_{n,\text{dis}} = \begin{cases} C\phi, & \text{if } s_{\max} > 0 \text{ and } c < c_{\max}, \\ 0, & \text{otherwise.} \end{cases} \quad (25)$$

The dynamics of the maximal saturation s_{\max} used to model hysteresis is represented using two different equations. The first equation describes how dissolution of CO_2 that is residually trapped below the free plume causes s_{\max} to decay

$$\frac{\partial b_n s_{\max}}{\partial t} = -q_{n,\text{dis}}, \text{ if } s_{\max} > s_n, \quad (26)$$

whereas the second equation states that s_{\max} increases with s_n in regions where CO_2 is invading or stagnant,

$$\frac{\partial s_{\max}}{\partial t} = \frac{\partial s_n}{\partial t}, \text{ if } s_{\max} = s_n. \quad (27)$$

Note that s_{\max} can never be less than s_n by definition. We call this the *rate-dependent dissolution model*.

Example 4. *To include compressibility effects, we move our 1D aquifer to a depth between 1300 and 850 meters. Figure 14 shows the evolution of the CO_2 plume for the case with rate-dependent dissolution and a top surface without small-scale undulations. Figure 16 illustrates how small-scale caprock undulations can effect the plume dynamics. In the top plot, we see how the interplay between undulations and tilt angle gives areas with very thin plume. To resolve these variations in an upscale sense, the effective relative permeability curves discussed in Example 3 obviously should be spatially*

²Here, hysteresis refers to the vertically-integrated equations and should not be confused with path-dependence between different imbibition and drainage curves in the fine-scale relative permeability and capillary functions, which is discussed in more detail in [50, 36, 37, 38]. Because of the sharp-interface assumption, only the end states of the bounding curves enter the equations.

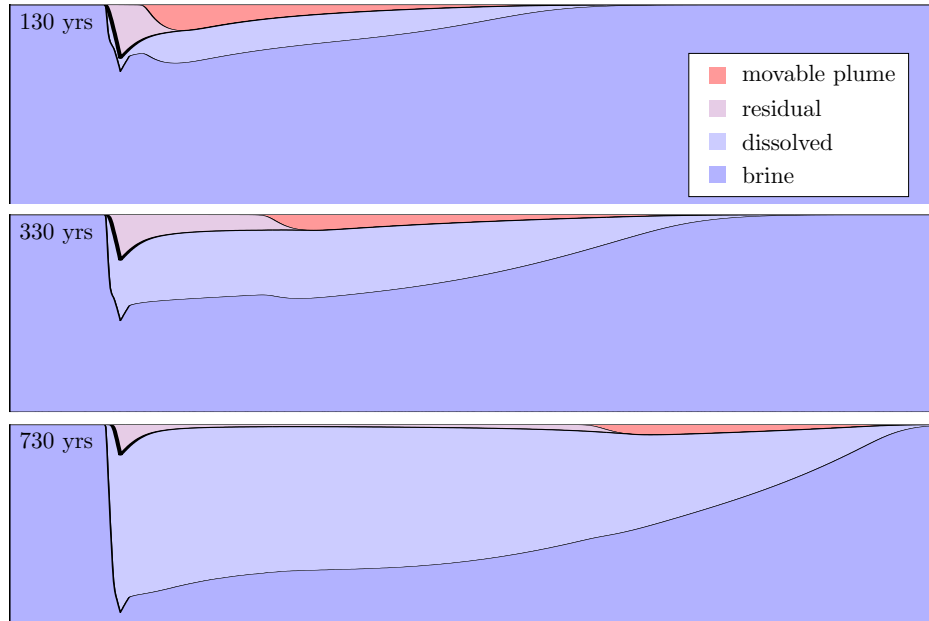


Figure 14: Evolution of the CO_2 distribution for $D = 1300$ m, $A = 0$, residual saturation, and rate-dependent dissolution. (From `dissolutionExample.m`.)

dependent. In the bottom plot, we see that the residually trapped CO_2 is converted to dissolved CO_2 except near the well, whereas near the tip of the plume, most of the CO_2 is trapped inside the small-scale undulations. Finally, Figure 15 compares the flowing CO_2 computed by different VE models and shows how small-scale undulations retard the plume migration, whereas residual trapping and dissolution both reduce the thickness of the plume; dissolution also reduces the thickness of the layer of residual CO_2 .

In the next example, we will compare the instantaneous and rate-dependent dissolution models on the Pliocenesand model.

Example 5. The Pliocenesand formation introduced in Example 2 is assumed to have a burial depth of at least 1200 meters and a rock compressibility of 10^{-5} bar^{-1} . An annual amount of 5 Mt/year is injected over 50 years from a single injection well located at model coordinates (485, 6647) km. Both brine and CO_2 are compressible: brine has constant compressibility equal $4.3 \cdot 10^{-5} \text{ bar}^{-1}$, whereas the density of the CO_2 follows the Span & Wagner PVT model [51] as computed by the open-source `coolprop` package

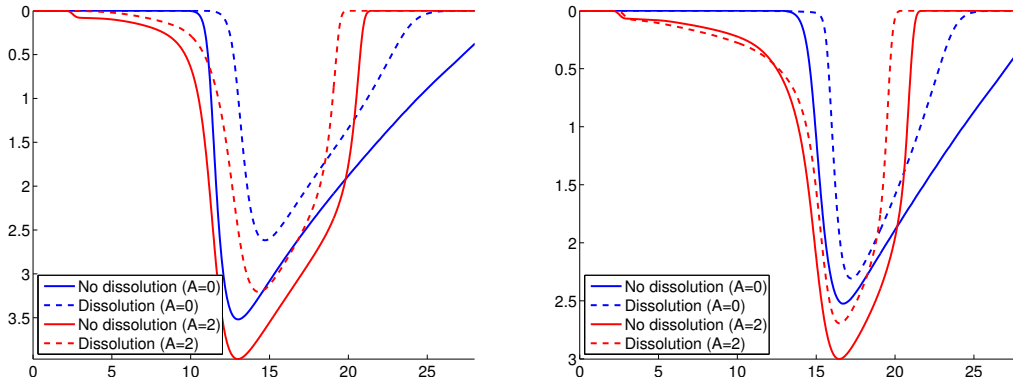


Figure 15: The flowing CO₂ phase 900 years after the injection has stopped. Dashed/solid lines denote models with/without rate-dependent dissolution, whereas red/blue colors signify cases with/without small-scale caprock undulations. The residual saturation is $s_{w,r} = 0$ to the left and $s_{w,r} = 0.2$ to the right. (From `dissolutionExample.m`.)

[67] with surface density equal 760 kg/m^3 . The dissolution process is assumed to either be non-existent, instantaneous, or follow (25) with $C = 0.05 \text{ m/year}$ and $c_{\max} = 0.03$. This gives is a value which is in the range estimated in the literature [56, 68, 57]. Figure 17 illustrates how one can conceptually think of the fluid distributions in the three resulting sharp-interface models.

Figure 18 shows two snapshots of the evolution of the CO₂ plume along with detailed carbon inventories resulting from the three different simulation models. Several interesting effects can be observed: Without dissolution, the plume will leave behind a relatively large amount of residual CO₂ as it propagates in the upslope direction. After approximately 750 years, the tip of the plume has reached the outskirts of the flat plain (seen to the left in the two snapshots) and starts to exit the simulated domain through the open boundary. After 3000 years, 24% of the injected CO₂ has left the formation, 20% is still free to move, while the remaining 56% can be considered safely stored. With instantaneous dissolution, on the other hand, a large fraction of the injected CO₂ will be dissolved and this will retard the plume migration so that the tip of the plume does not reach the open boundaries within the simulation period. After 3000 years, 99.6% of the injected CO₂ can be considered safely stored. With rate-dependent resolution, the retardation effect is much less than with instantaneous dissolution and the tip of the plume therefore reaches the outer boundary after approximately 1500 years

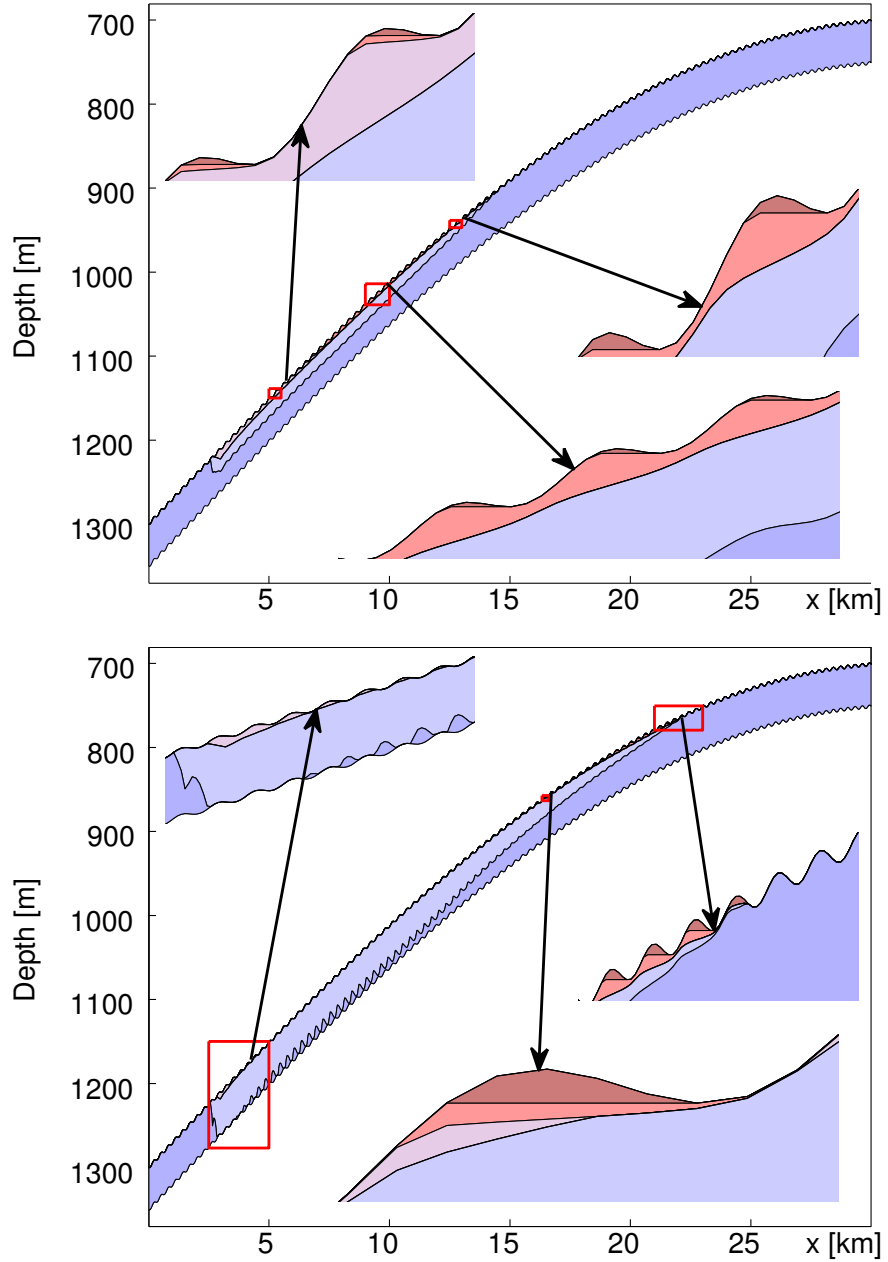


Figure 16: The CO₂ distribution in global coordinates after 330 years (top) and after 930 years (bottom) for the case with compressibility, residual saturation, and rate-dependent dissolution. (From `dissolutionExample1.m`.)

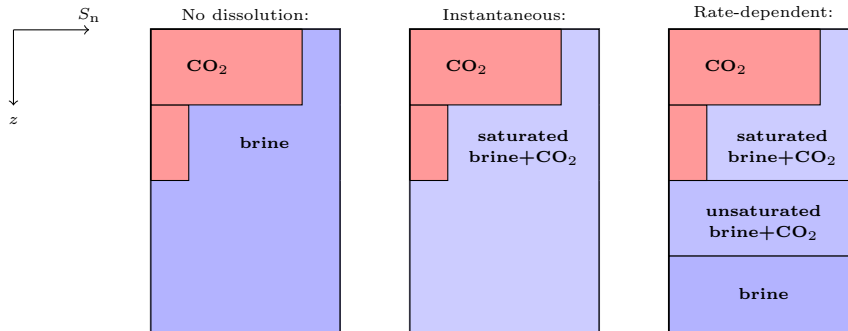


Figure 17: Conceptual fluid distribution in the three different sharp-interface models used to study the effects of dissolution on the Pliocenesand formation. (In reality, the CO_2 -saturated brine will be denser than the resident brine and hence sink to the bottom).

and starts to leak. By comparing the two upper plots, we also see that the gradual dissolution causes the extent of the residual CO_2 to retract during the 500 year period between the snapshots. After 3000 years, 78% of the injected CO_2 is dissolved, 6% is residually trapped, 0.8% has leaked, and 11% is still free to move. The total CPU times for the three simulations are 189, 425, and 1118 seconds, respectively, on an Intel Xeon 3.47GHz CPU. For the rate-dependent simulation, a large number of time-step cuts contribute to the high computational cost.

Finally, we remark that we have so far not considered lateral transport of CO_2 dissolved in brine induced by density differences. To model this effect, one has to introduce different velocities for water with CO_2 and water without CO_2 . Our models did not include this effect since it is approximately one thousand times slower than the movement of the CO_2 plume: a factor one hundred is caused by less density difference with water, and a factor ten can be attributed to the larger viscosity compared to CO_2 . However, transport of dissolved CO_2 may be important from a numerical point-of-view because without this effect there is no physical diffusion to smooth out and stabilize the concentration c . Making the other approximation based on putting the denser CO_2 -rich water just below the CO_2 plume, which is the mental picture made when introducing convection-enhanced dissolution, will lead to a negative diffusion term that may amplify oscillations.

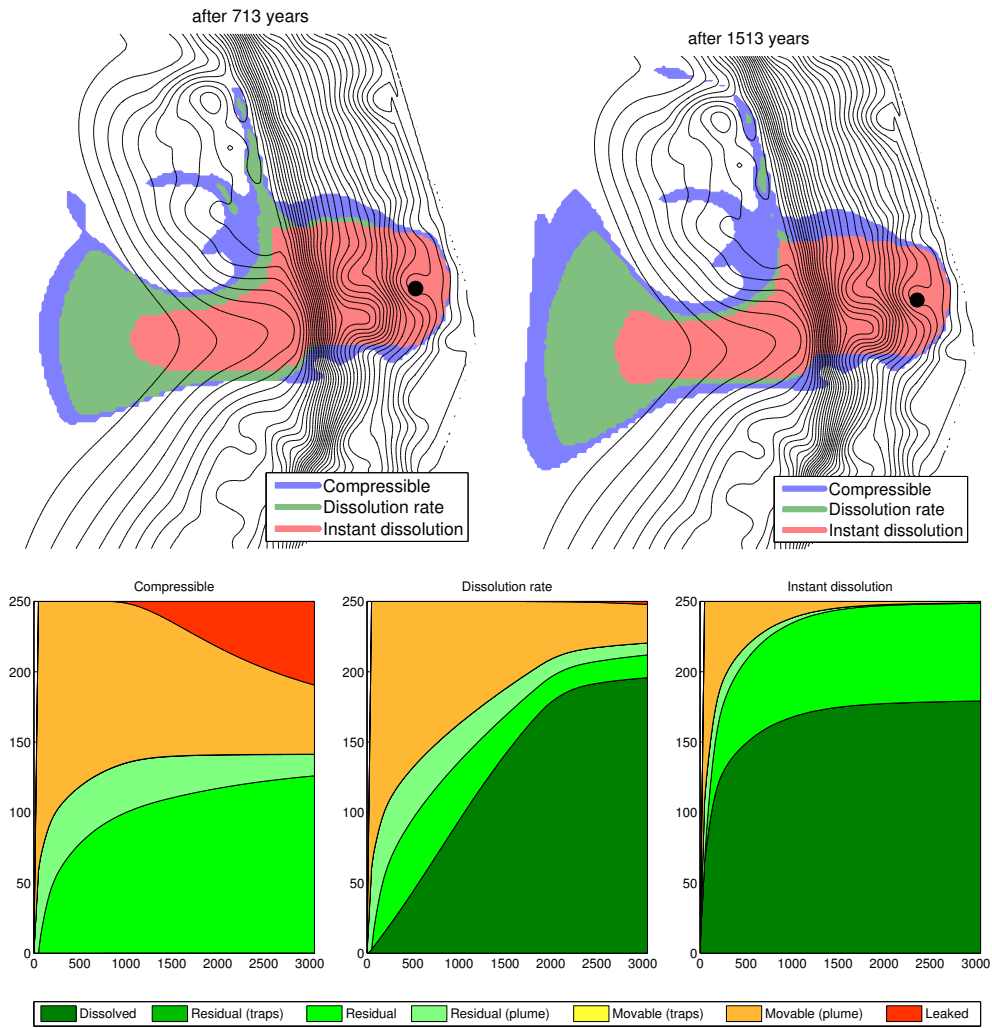


Figure 18: Modeling the effects of dissolution on the CO₂ migration for a single injection point in the Pliocenesand formation. The upper plots show the extent of the residual CO₂ at two different instances in time computed by models without dissolution, with instantaneous dissolution, and with rate-dependent dissolution. The lower plots show the corresponding carbon inventories (in units mega-tonnes and years since injection started). (From `secondPlioExample.m` and `showSecondPlioExample.m`.)

5. Choice of numerical methods

The VE models discussed above have the same structure as traditional equations for multiphase flow in porous media. The dominant discretization within reservoir simulation is the fully-implicit method with phase-based upstream-mobility weighting and two-point flux approximation. Alternatively, one can use the implicit pressure, explicit saturation (IMPES) method, in which the time step is limited by the CFL restriction on the explicit saturation update, or a sequential splitting that combines a pressure solver with an appropriate explicit or (semi-)implicit saturation solver. Several commercial simulators have vertical-equilibrium options that work with both fully-implicit and sequential solvers (see e.g., [27, 69]). This option has been added both to improve computational performance and numerical accuracy for thin and/or well-segregated reservoirs. However, none of these simulators can incorporate all the model features discussed herein. Conversely, most research codes used in the literature to study CO₂ migration are based on a simple IMPES or sequential-splitting method and are not publicly available. In particular, the VESA code [26], which to the best of our knowledge is the most general code reported in the literature, uses a nonstandard non-conservative version of IMPES, but nevertheless seems to work rather well.

We have previously used sequential splitting methods for the simplified incompressible models discussed in Section 3, and this choice has proved to be both efficient and robust in the sense that these methods produce stable solutions [27, 33]. In [42], we also pointed out that the coupling between pressure and transport tends to be weak for migration-type scenarios formulated in a VE framework compared to a standard 3D simulation. Also for more complex models, our experience is that the combination of stable splitting methods (e.g., as discussed in [70]) with explicit and highly parallel transport solvers [71, 72] will efficiently resolve the primary flow effects for a range of relevant resolutions. This approach is particularly efficient for rectilinear grids with coarse resolutions like seen in the CO₂ Storage Atlas of the Norwegian Continental Shelf [14].

On the other hand, sequential and explicit methods have limitations on fine grids and for almost stationary states. In particular, the gravity effect that creates a flat CO₂ interface (e.g., inside a structural trap) turns up as a second-order term in the transport equation, similar to how capillary forces appear in traditional reservoir simulation. As a result, the transport equation will have a strong parabolic character and will be more tightly coupled to

the pressure equations. It is well known within the reservoir simulation community that spatially-dependent and strong capillary pressure is best simulated using fully-implicit methods, since a tight coupling of pressure and transport will reduce the stability and put severe restrictions on the time step of IMPES and other sequential-splitting methods. Implicit methods can also be preferable during the injection stage since they have the ability to take long time steps. An example of such behavior was illustrated in Figure 10.

For all these reasons, `MRST-co2lab` offers two different types of solvers: (i) sequential-splitting methods with explicit or implicit transport solvers to provide efficient solution of the basic model discussed in Section 3, and (ii) fully-implicit solvers for VE formulations that can easily handle steady-states and incorporate more physical flow effects like compressibility, hysteresis, and dissolution as discussed in Section 4. To the best of our knowledge, fully-implicit VE solvers that include all the main trapping mechanisms have not been reported previously in the literature. We believe that such solvers are particularly important to efficiently and robustly resolve the important stationary states of flat CO₂ interfaces. The fully-implicit solvers in `MRST-co2lab` are implemented using automatic differentiation [12], which makes it straightforward to compute gradients from adjoint equations. Having gradients is important to determine parameter sensitivities or if one wants to use rigorous mathematical optimization methods to propose plausible injection points and strategies.

Acknowledgments

The work was funded in part by Statoil ASA and the Research Council of Norway through grants no. 199878 (Numerical CO₂ laboratory), 215641 (MatMoRA-II), 243729 (Simulation and optimization of large-scale, aquifer-wide CO₂ injection in the North Sea).

References

- [1] H. Class, A. Ebigbo, R. Helmig, H. K. Dahle, J. M. Nordbotten, M. A. Celia, P. Audigane, M. Darcis, J. Ennis-King, Y. Fan, B. Flemisch, S. E. Gasda, M. Jin, S. Krug, D. Labregere, A. N. Beni, R. J. Pawar, A. Sbai, S. G. Thomas, L. Trenty, L. Wei, A benchmark study on problems related to CO₂ storage in geologic formations, *Comput. Geosci.* 13 (4) (2009) 409–434. doi:10.1007/s10596-009-9146-x.

- [2] G. Eigestad, H. Dahle, B. Hellevang, F. Riis, W. Johansen, E. Øian, Geological modeling and simulation of CO₂ injection in the Johansen formation, *Comput. Geosci.* 13 (4) (2009) 435–450. doi:10.1007/s10596-009-9153-y.
- [3] G. Eigestad, H. Dahle, B. Hellevang, W. Johansen, K.-A. Lie, F. Riis, E. Øian, Geological and fluid data for modelling CO₂ injection in the Johansen formation (2008).
URL <http://www.sintef.no/Projectweb/MatMorA/Downloads/Johansen>
- [4] SINTEF ICT, The MATLAB Reservoir Simulation Toolbox: Numerical CO₂ laboratory (Oct. 2014).
URL <http://www.sintef.no/co2lab>
- [5] H. M. Nilsen, K.-A. Lie, O. Møyner, O. Andersen, Spill-point analysis and structural trapping capacity in saline aquifers using MRST-co2lab, *Computers & Geoscience* 75 (2015) 33–43. doi:10.1016/j.cageo.2014.11.002.
- [6] H. M. Nilsen, K.-A. Lie, O. Andersen, Analysis of trapping capacities in the Norwegian North Sea using MRST-co2lab, *Computers & Geoscience* 79 (2015) 15–26. doi:10.1016/j.cageo.2015.03.001.
- [7] K.-A. Lie, H. M. Nilsen, O. Andersen, O. Møyner, A simulation workflow for large-scale CO₂ storage in the Norwegian North Sea, *Comput. Geosci.* (2015) 1–16. doi:10.1007/s10596-015-9487-6.
- [8] O. Andersen, K.-A. Lie, H. M. Nilsen, An open-source toolchain for simulation and optimization of aquifer-wide CO₂ storage, *Energy Procedia* (2015) 1–10, the 8th Trondheim Conference on Capture, Transport and Storage.
- [9] The MATLAB Reservoir Simulation Toolbox, version 2015a, <http://www.sintef.no/MRST/> (May 2015).
- [10] K.-A. Lie, S. Krogstad, I. S. Ligaarden, J. R. Natvig, H. M. Nilsen, B. Skaflestad, Open source MATLAB implementation of consistent discretisations on complex grids, *Comput. Geosci.* 16 (2012) 297–322. doi:10.1007/s10596-011-9244-4.

- [11] K.-A. Lie, An Introduction to Reservoir Simulation Using MATLAB: User guide for the Matlab Reservoir Simulation Toolbox (MRST), SINTEF ICT, <http://www.sintef.no/Projectweb/MRST/publications>, 1st Edition (May 2014).
- [12] S. Krogstad, K.-A. Lie, O. Møyner, H. M. Nilsen, X. Raynaud, B. Skaflestad, MRST-AD – an open-source framework for rapid prototyping and evaluation of reservoir simulation problems, in: SPE Reservoir Simulation Symposium, 23–25 February, Houston, Texas, 2015. doi:10.2118/173317-MS.
- [13] International Energy Agency, Sleipner benchmark model (2012). URL <http://www.ieaghg.org/index.php?/2009112025/modelling-network.html>
- [14] E. K. Halland, J. Mujezinović, F. Riis (Eds.), CO₂ Storage Atlas: Norwegian Continental Shelf, Norwegian Petroleum Directorate, P.O. Box 600, NO-4003 Stavanger, Norway, 2014. URL <http://www.npd.no/en/Publications/Reports/Compiled-CO2-atlas/>
- [15] J. C. Martin, Some mathematical aspects of two phase flow with application to flooding and gravity segregation, *Prod. Monthly* 22 (6) (1958) 22–35.
- [16] K. H. Coats, R. L. Nielsen, M. H. Terune, A. G. Weber, Simulation of three-dimensional, two-phase flow in oil and gas reservoirs, *Soc. Pet. Eng. J. Dec* (1967) 377–388.
- [17] J. C. Martin, Partial integration of equation of multiphase flow, *Soc. Pet. Eng. J. Dec* (1968) 370–380.
- [18] K. H. Coats, J. R. Dempsey, J. H. Henderson, The use of vertical equilibrium in two-dimensional simulation of three-dimensional reservoir performance, *Soc. Pet. Eng. J. Mar* (1971) 68–71.
- [19] J. M. Nordbotten, M. A. Celia, *Geological Storage of CO₂: Modeling Approaches for Large-Scale Simulation*, John Wiley & Sons, Hoboken, New Jersey, 2012.
- [20] Y. Yortsos, A theoretical analysis of vertical flow equilibrium, *Transp. Porous Media* 18 (2) (1995) 107–129. doi:10.1007/BF01064674.

- [21] B. Court, K. W. Bandilla, M. A. Celia, A. Janzen, M. Dobossy, J. M. Nordbotten, Applicability of vertical-equilibrium and sharp-interface assumptions in CO₂ sequestration modeling, *International Journal of Greenhouse Gas Control* 10 (2012) 134–147. doi:10.1016/j.ijggc.2012.04.015.
- [22] K. W. Bandilla, M. A. Celia, J. T. Birkholzer, A. Cihan, E. C. Leister, Multiphase modeling of geologic carbon sequestration in saline aquifers, *Groundwater* 53 (3) (2015) 362–377. doi:10.1111/gwat.12315.
- [23] M. A. Celia, S. Bachu, J. M. Nordbotten, K. W. Bandilla, Status of CO₂ storage in deep saline aquifers with emphasis on modeling approaches and practical simulations, *Water Resources Research* 51 (9). doi:10.1002/2015WR017609.
- [24] J. M. Nordbotten, M. A. Celia, Similarity solutions for fluid injection into confined aquifers, *J. Fluid Mech.* 561 (2006) 307–327. doi:10.1017/S0022112006000802.
- [25] M. A. Hesse, F. M. Orr, H. A. Tchelepi, Gravity currents with residual trapping, *J. Fluid. Mech.* 611 (2008) 35–60.
- [26] S. E. Gasda, J. M. Nordbotten, M. A. Celia, Vertical equilibrium with sub-scale analytical methods for geological CO₂ sequestration, *Comput. Geosci.* 13 (4) (2009) 469–481. doi:10.1007/s10596-009-9138-x.
- [27] H. M. Nilsen, P. A. Herrera, M. Ashraf, I. Ligaarden, M. Iding, C. Hermanrud, K.-A. Lie, J. M. Nordbotten, H. K. Dahle, E. Keilegavlen, Field-case simulation of CO₂-plume migration using vertical-equilibrium models, *Energy Procedia* 4 (0) (2011) 3801–3808. doi:10.1016/j.egypro.2011.02.315.
- [28] S. E. Gasda, J. M. Nordbotten, M. A. Celia, Application of simplified models to CO₂ migration and immobilization in large-scale geological systems, *Int. J. Greenh. Gas Control* 9 (2012) 72–84. doi:10.1016/j.ijggc.2012.03.001.
- [29] O. Andersen, S. Gasda, H. M. Nilsen, Vertically averaged equations with variable density for CO₂ flow in porous media, *Transp. Porous Media* 107 (2015) 95–127. doi:10.1007/s11242-014-0427-z.

- [30] S. E. Gasda, J. M. Nordbotten, M. A. Celia, Vertically-averaged approaches to CO₂ injection with solubility trapping, *Water Resources Research* 47 (2011) W05528. doi:10.1029/2010WR009075.
- [31] T. S. Mykkeltvedt, J. M. Nordbotten, Estimating effective rates of convective mixing from commercial-scale injection, *Environ. Earth Sci.* 67 (2) (2012) 527–535. doi:10.1007/s12665-012-1674-3.
- [32] J. M. Nordbotten, H. K. Dahle, Impact of the capillary fringe in vertically integrated models for CO₂ storage, *Water Resour. Res.* 47 (2) (2011) W02537. doi:10.1029/2009WR008958.
- [33] H. M. Nilsen, A. R. Syversveen, K.-A. Lie, J. Tveranger, J. M. Nordbotten, Impact of top-surface morphology on CO₂ storage capacity, *Int. J. Greenh. Gas Control* 11 (0) (2012) 221–235. doi:10.1016/j.ijggc.2012.08.012.
- [34] S. E. Gasda, H. M. Nilsen, H. K. Dahle, W. G. Gray, Effective models for CO₂ migration in geological systems with varying topography, *Water Resour. Res.* 48 (10). doi:10.1029/2012WR012264.
- [35] S. E. Gasda, H. M. Nilsen, H. K. Dahle, Impact of structural heterogeneity on upscaled models for large-scale CO₂ migration and trapping in saline aquifers, *Adv. Water Resour.* 62, Part C (0) (2013) 520–532. doi:10.1016/j.advwatres.2013.05.003.
- [36] S. E. Gasda, E. du Plessis, H. K. Dahle, Upscaled models for modeling CO₂ injection and migration in geological systems, in: P. Bastian, J. Kraus, R. Scheichl, M. Wheeler (Eds.), *Simulation of Flow in Porous Media*, Vol. 12 of Radon Series on Computational and Applied Mathematics, De Gruyter, Berlin, Boston, 2013, pp. 1–38. doi:10.1515/9783110282245.1.
- [37] F. Doster, J. M. Nordbotten, M. A. Celia, Hysteretic upscaled constitutive relationships for vertically integrated porous media flow, *Comput. Visual. Sci.* 15 (2012) 147–161. doi:10.1007/s00791-013-0206-3.
- [38] F. Doster, J. Nordbotten, M. Celia, Impact of capillary hysteresis and trapping on vertically integrated models for CO₂ storage, *Adv. Water Resour.* 62, Part C (2013) 465–474. doi:10.1016/j.advwatres.2013.09.005.

- [39] K. W. Bandilla, M. A. Celia, T. R. Elliot, M. Person, K. M. Ellett, J. A. Rupp, C. Gable, Y. Zhang, Modeling carbon sequestration in the illinois basin using a vertically-integrated approach, *Comput. Vis. Sci.* 15 (1) (2012) 39–51. doi:10.1007/s00791-013-0195-2.
- [40] K. W. Bandilla, S. R. Kraemer, J. T. Birkholzer, Using semi-analytic solutions to approximate the area of potential impact for carbon dioxide injection, *Int. J. Greenh. Gas Control* 8 (2012) 196–204. doi:10.1016/j.ijggc.2012.02.009.
- [41] S. Gasda, A. Stephansen, I. Aavatsmark, H. Dahle, Upscaled modeling of CO₂ injection and migration with coupled thermal processes, *Energy Procedia* 40 (2013) 384–391. doi:10.1016/j.egypro.2013.08.044.
- [42] I. S. Ligaarden, H. M. Nilsen, Numerical aspects of using vertical equilibrium models for simulating CO₂ sequestration, in: *Proceedings of ECMOR XII–12th European Conference on the Mathematics of Oil Recovery*, EAGE, Oxford, UK, 2010.
- [43] K. W. Bandilla, M. A. Celia, E. Leister, Impact of model complexity on CO₂ plume modeling at Sleipner, *Energy Procedia* 63 (2014) 3405–3415, 12th International Conference on Greenhouse Gas Control Technologies, GHGT-12. doi:10.1016/j.egypro.2014.11.369.
- [44] H. H. Jacks, O. J. E. Smith, C. C. Mattax, The modeling of a three-dimensional reservoir with a two-dimensional reservoir simulator – the use of dynamic pseudo functions, *Soc. Pet. Eng. J.* 13 (3) (1973) 175–185. doi:10.2118/4071-PA.
- [45] J. R. Kyte, D. W. Berry, New pseudo functions to control numerical dispersion, *Soc. Pet. Eng. J.* 15 (4) (1975) 269–276. doi:10.2118/5105-PA.
- [46] H. L. Stone, Rigorous black oil pseudo functions, in: *SPE Symposium on Reservoir Simulation*, 17-20 February, Anaheim, California, Society of Petroleum Engineers, 1991. doi:10.2118/21207-MS.
- [47] J. Barker, S. Thibeau, A critical review of the use of pseudorelative permeabilities for upscaling, *SPE Reservoir Engineering* 12 (2) (1997) 138–143. doi:10.2118/35491-PA.

- [48] O. Andersen, H. M. Nilsen, K.-A. Lie, Reexamining CO₂ storage capacity and utilization of the Utsira Formation, in: ECMOR XIV – 14th European Conference on the Mathematics of Oil Recovery, Catania, Sicily, Italy, 8-11 September 2014, EAGE, 2014. doi:10.3997/2214-4609.20141809.
- [49] K.-A. Lie, H. M. Nilsen, O. Andersen, O. Møyner, A simulation workflow for large-scale CO₂ storage in the Norwegian North Sea, in: ECMOR XIV – 14th European Conference on the Mathematics of Oil Recovery, Catania, Sicily, Italy, 8-11 September 2014, EAGE, 2014. doi:10.3997/2214-4609.20141877.
- [50] H. M. Nilsen, K.-A. Lie, O. Andersen, Fully implicit simulation of vertical-equilibrium models with hysteresis and capillary fringe, *Comput. Geosci.* (2015) .
- [51] R. Span, W. Wagner, A new equation of state for carbon dioxide covering the fluid region from triple-point temperature to 1100 K at pressures up to 800 MPa, *J. Phys. Chem. Ref. Data* 25 (6) (1996) 1509–1597.
- [52] R. Juanes, C. W. MacMinn, M. L. Szulczewski, The footprint of the CO₂ plume during carbon dioxide storage in saline aquifers: Storage efficiency for capillary trapping at the basin scale, *Transp. Porous Media* 82 (1) (2010) 19–30. doi:10.1007/s11242-009-9420-3.
- [53] E. K. Halland, W. T. Johansen, F. Riis (Eds.), CO₂ Storage Atlas: Norwegian North Sea, Norwegian Petroleum Directorate, P. O. Box 600, NO-4003 Stavanger, Norway, 2011.
URL <http://www.npd.no/no/Publikasjoner/Rapporter/CO2-lagringsatlas/>
- [54] H. Hoteit, A. Firoozabadi, Numerical modeling of two-phase flow in heterogeneous permeable media with different capillarity pressures, *Adv. Water Resour.* 31 (1) (2008) 56–73. doi:10.1016/j.advwatres.2007.06.006.
- [55] P. Renard, G. De Marsily, Calculating equivalent permeability: a review, *Adv. Water Resour.* 20 (5) (1997) 253–278.
- [56] A. Riaz, M. Hesse, H. A. Tchelepi, F. M. Orr, Onset of convection in a gravitationally unstable diffusive boundary layer in porous media, *J. Fluid. Mech.* 548 (2006) 87–111. doi:10.1017/S0022112005007494.

- [57] G. S. H. Pau, J. B. Bell, K. Pruess, A. S. Almgren, M. J. Lijewski, K. Zhang, High-resolution simulation and characterization of density-driven flow in CO₂ storage in saline aquifers, *Adv. Water Resour.* 33 (4) (2010) 443–455. doi:10.1016/j.advwatres.2010.01.009.
- [58] H. Hassanzadeh, M. Pooladi-Darvish, D. W. Keith, Scaling behavior of convective mixing, with application to geological storage of CO₂, *AIChE J.* 53 (5) (2007) 1121–1131. doi:10.1002/aic.11157.
- [59] M. T. Elenius, Convective mixing in geological carbon storage, Ph.D. thesis, University of Bergen (2011).
URL <https://bora.uib.no/handle/1956/5540>
- [60] P. Cheng, M. Bestehorn, A. Firoozabadi, Effect of permeability anisotropy on buoyancy-driven flow for CO₂ sequestration in saline aquifers, *Water Resour. Res.* 48 (9). doi:10.1029/2012WR011939.
- [61] H. Alnes, O. Eiken, S. Nooner, G. Sasagawa, T. Stenvold, M. Zumberge, Results from Sleipner gravity monitoring: Updated density and temperature distribution of the CO₂ plume, *Energy Procedia* 4 (0) (2011) 5504–5511, 10th International Conference on Greenhouse Gas Control Technologies. doi:10.1016/j.egypro.2011.02.536.
- [62] V. L. Hauge, O. Kolbjørnsen, Bayesian inversion of gravimetric data and assessment of CO₂ dissolution in the utsira formation, *Interpretation* 3 (2) (2015) SP1–SP10. doi:10.1190/INT-2014-0193.1.
- [63] R. L. Van Dam, C. T. Simmons, D. W. Hyndman, W. W. Wood, Natural free convection in porous media: First field documentation in groundwater, *Geophys. Res. Lett.* 36 (11). doi:10.1029/2008GL036906.
- [64] R. L. Van Dam, B. P. Eustice, D. W. Hyndman, W. W. Wood, C. T. Simmons, Electrical imaging and fluid modeling of convective fingering in a shallow water-table aquifer, *Water Resour. Res.* 50 (2) (2014) 954–968. doi:10.1002/2013WR013673.
- [65] M. P. Anderson, Heat as a ground water tracer, *Ground Water* 43 (6) (2005) 951–968. doi:10.1111/j.1745-6584.2005.00052.x.

- [66] M. . Saar, Review: Geothermal heat as a tracer of large-scale ground-water flow and as a means to determine permeability fields, *Hydrogeol. J.* 19 (1) (2011) 31–52. doi:10.1007/s10040-010-0657-2.
- [67] I. H. Bell, J. Wronski, S. Quoilin, V. Lemort, Pure and Pseudo-pure Fluid Thermophysical Property Evaluation and the Open-Source Thermophysical Property Library CoolProp, *Ind. Eng. Chem. Res.* 53 (6) (2014) 2498–2508. doi:10.1021/ie4033999.
- [68] S. M. Benson, et al., Underground geological storage, in: *IPCC Special Report on Carbon Dioxide Capture and Storage*, Intergovernmental Panel on Climate Change, Cambridge University Press, Cambridge, U.K., 2005, Ch. 5.
- [69] A. Cavanagh, Benchmark calibration and prediction of the Sleipner CO₂ plume from 2006 to 2012, *Energy Procedia* 37 (2013) 3529–3545, gHGT-11. doi:10.1016/j.egypro.2013.06.246.
- [70] K.-A. Lie, H. M. Nilsen, A. F. Rasmussen, X. Raynaud, Fast simulation of polymer injection in heavy-oil reservoirs based on topological sorting and sequential splitting, *SPE J.* 19 (6) (2014) 991–1004. doi:10.2118/163599-PA.
- [71] M. Ertsås, Vertically integrated models of CO₂ migration: GPU accelerated simulations, Master’s thesis, University of Oslo (2011). URL <http://urn.nb.no/URN:NBN:no-28112>
- [72] E. K. Prestegård, A GPU accelerated simulator for CO₂ storage, Master’s thesis, Norwegian University of Science and Technology (2014). URL <https://daim.idi.ntnu.no/masteroppgave?id=10345>

Appendix A. Change of coordinate systems

In Section 3, we derived a transport equation on the form

$$\frac{\partial}{\partial t}\Phi(h) + \nabla_{\parallel} \left[\mathbf{F}_n(h)\vec{V} + \mathbf{G}_n(h)[\vec{g}_{\parallel} + g_{\zeta}\nabla_{\parallel}(Z + h)] \right] = Q_n,$$

which involves operators ∇_{\parallel} that are defined relative to a rotated coordinate system that locally aligns with the top surface of the aquifer. The disadvantage of operating in this curvilinear coordinate system is that it is difficult to

calculate volumes and that the absolute height of the CO₂ surface will depend on geometric interpretations. The latter is a disadvantage since a stationary state without driving forces, which in physical space is a horizontal interface between CO₂ and brine, will generally not correspond to a constant value of $h(\xi, \eta)$. Hence, it is more complicated to derive numerical schemes that honor this important physical property exactly. In our implementation, we have therefore chosen to work with transport equations formulated directly in the original physical coordinate system. This will potentially introduce two errors.

The first error is associated with the approximation $\nabla_{\parallel} \approx \nabla_{xy}$, which results in an error of the order θ^2 . However, for the important stationary case we have equilibrium in all directions so the VE assumption will in fact be exact in the new coordinate system. Also for plumes of significant thickness, the interface between CO₂ and water will be near horizontal and assuming equilibrium in the vertical direction will be an approximation that is at least as good as assuming equilibrium in the direction perpendicular to the top surface.

The second error comes from a change of geometry in our interpretation of the physical quantities. In the original formulation, the height h is defined relative to the vector \vec{e}_{ζ} , which is constant if we use a coordinate system aligned with the mean dip angle and variable if we use a curvilinear coordinate system that follows the top surface. When working in the physical coordinates, the height value will be interpreted in the z -direction. Hence, we will calculate the volume of CO₂ by $h_z A_{xy}$ and interpret all lengths as measured in the xy plane, see Figure A.19. For a planar surface, we have that $A_{xy} = A_{\xi\eta} \cos \theta$ and $h_{\zeta} = h_z \cos \theta$, from which it follows that the volume is preserved. For a curved surface, the volume attached to each surface patch will generally be a function for which the side faces are not fully aligned with \vec{e}_{ζ} . Replacing this by a cuboid aligned with the physical coordinates will introduce an error. The bottom plot in Figure A.19 illustrates this; here the column is a trapezoid with sides that deviate an angle $\theta_{12} = \frac{1}{2}(\theta_1 - \theta_2)$ and $\theta_{23} = \frac{1}{2}(\theta_2 - \theta_3)$, respectively from being a rectangular. By replacing this trapezoid by a rectangular with the same base and height, we make the

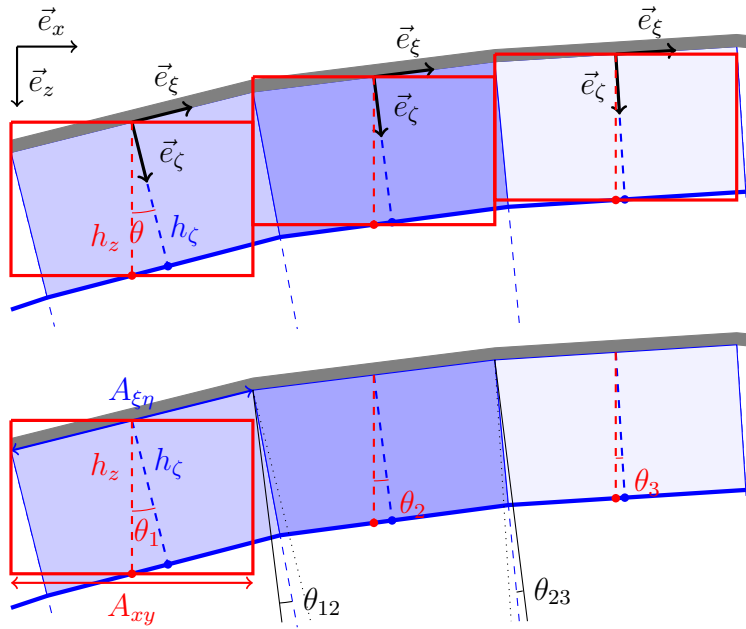


Figure A.19: Approximation of the column geometry for a plume (thick blue line) under a sloping caprock (thick gray line). The depth of the plume is defined pointwise for each ξ in the direction of the vector \vec{e}_ζ . For a discrete grid model, this gives volumes as shown by the blue boxes that can be associated with the centroids of the surface grid. To simplify the calculation, we reinterpret this volume as being along vertical pillars along \vec{e}_z , as shown by the red boxes. (The aspect ratios in the figures are greatly exaggerated for illustration purposes; typical θ values are a few degrees.)

following error per unit distance

$$\begin{aligned}
\frac{\Delta V}{\Delta x} &= \frac{1}{2} \frac{h^2}{\Delta x} [\tan \theta_{12} + \tan \theta_{23}] \\
&= \frac{1}{2} \frac{h^2}{\Delta x} \left[\tan\left(\frac{1}{2}(\theta_1 - \theta_2)\right) + \tan\left(\frac{1}{2}(\theta_2 - \theta_3)\right) \right] \\
&\approx \frac{1}{2} \frac{h^2}{\Delta x} \left[\frac{1}{2}(\theta_1 - \theta_2) + \frac{1}{2}(\theta_2 - \theta_3) \right] \\
&= \frac{1}{2} h^2 \frac{\theta_1 - \theta_3}{2\Delta x} \approx -\frac{1}{2} h^2 \frac{\partial \theta}{\partial x}.
\end{aligned}$$

In other words, we get an error depending on the second derivative of the top surface. The approximation we have adopted is valid for small tilt angles θ and small curvature. It greatly simplifies the numerical code and processing of the grid since there is no need to introduce the local coordinate system. For realistic models, the spatial dimensions are generally working in our favor: grid cells will typically have lengths of the order 100–1000 meters, the total height of an aquifer will at most be a few hundred meters, and the mean dip angle up to a few degrees.

In the derivation of the equations, we have integrated the permeability and porosity in the ζ -direction. In the cases where heterogeneity in the vertical direction is considered, we integrate in the z -direction, or more precisely in the direction of the grid column in the case of corner-point grids, and assume that the main flow will take place in the xy direction. Alternatively, we could integrate vertically at the start, assuming hydrostatic distribution in the vertical direction. This, however, introduces an error proportional to $\theta|v|$, where $|v|$ is the Darcy flow velocity. The end result of the derivation will be the same as we use, but the derivation will indicate a larger error of order $\mathcal{O}(\theta)$. For gravity driven flow, $|v|$ is of order $\mathcal{O}(\theta)$, which means that the pressure reconstruction is of order $\mathcal{O}(\theta^2)$. In addition, the pressure reconstruction is only used inside derivatives, and hence the error in the flux depends on the derivative of θ for constant $|v|$. This derivation is somewhat simpler when deriving the practical method, but we believe that our derivation gives a better description of the combined approximations of the VE assumptions and the numerical implementations in a realistic setting.

Appendix B. The black-oil equations

The predominant way of simulating multiphase flow in petroleum reservoirs is through the so-called 'black-oil model' in which various chemical species are lumped together to form two components at surface conditions, a denser 'oil' component and a lighter 'gas' component. At reservoir conditions, these two components can be partially or completely dissolved in each other depending on pressure and temperature, forming two hydrocarbon phases, a liquid oleic phase and or a gaseous phase, that may coexist with an aqueous phase.

By convention, the black-oil equations are formulated as conservation of the gas, oil, and water component at standard surface conditions combined with a simple PVT model that uses pressure-dependent functions to related fluid volumes at surface and reservoir conditions. To state the equations, we define the inverse formation-volume factors $b_\ell = V_\ell^s/V_\ell$, where V_ℓ^s and V_ℓ denote the volumes occupied by a bulk of component ℓ at surface and reservoir conditions, respectively. The solubility of gas in oil is usually modelled through the pressure-dependent solution gas-oil ratio, $r_{so} = V_g^s/V_o^s$ defined as the volume of gas, measured at standard conditions, that at reservoir conditions is dissolved in a unit of stock-tank oil. The black-oil framework also opens for oil vaporized in gas, and the presence of the hydrocarbon components in the aqueous phase and water in the gaseous and oleic phases, but these possibilities are not needed for our purpose herein. With this, we can now write the system of continuity equations for our three-component, three-phase system as:

$$\begin{aligned} \partial_t(\phi b_o s_o) + \nabla \cdot (b_o \vec{v}_o) - b_o q_o &= q_o, \\ \partial_t(\phi b_w s_w) + \nabla \cdot (b_w \vec{v}_w) - b_w q_w &= q_w, \\ \partial_t[\phi(b_g s_g + b_o r_{so} s_o)] + \nabla \cdot (b_g \vec{v}_g + b_o r_{so} \vec{v}_o) - (b_g q_g + b_o r_{so} q_o) &= q_g. \end{aligned}$$

In addition, we need various closure relationships, which particularly includes relations that express the capillary pressures as functions of phase saturations

$$p_o - p_w = P_{cow}(s_w, s_o), \quad p_g - p_o = P_{cgo}(s_o, s_g).$$